

1 **Tipping points in overturning circulation mediated by ocean mixing and the**
2 **configuration and magnitude of the hydrological cycle: A simple model**

3 Anand Gnanadesikan,^a Gianluca Fabiani,^b Jingwen Liu,^a Renske Gelderloos,^{a,c} G. Jay Brett^d
4 , Yannis Kevrekidis,^e Thomas Haine,^a Marie-Aude Pradal,^a Constantinos Siettos,^f and Jennifer
5 Sleeman,^d

6 ^a *Morton K. Blaustein Department of Earth and Planetary Science, Johns Hopkins University,
7 Baltimore, MD, USA*

8 ^b *Modeling Engineering Risk and Complexity, Scuola Superiore Meridionale, Naples, Italy*

9 ^c *Department of Hydraulic Engineering, Delft University of Technology, Delft, The Netherlands*
10 ^d *Johns Hopkins Applied Physics Lab, Laurel, MD, USA*

11 ^e *Department of Chemical Engineering, Johns Hopkins University, Baltimore, MD, USA*

12 ^f *Department of Applied Mathematics, University of Naples Federico II, Naples, Italy*

13 *Corresponding author: Anand Gnanadesikan, gnanades@jhu.edu*

¹⁴ ABSTRACT: In the modern ocean, transformation of light surface waters to dense deep waters
¹⁵ primarily occurs in the Atlantic basin rather than in the North Pacific or Southern Oceans. The
¹⁶ reasons for this remain unclear, as both models and paleoclimatic observations suggest that sinking
¹⁷ can sometimes occur in the Pacific. We present a six-box model of the overturning that combines
¹⁸ insights from a number of previous studies. A key determinant of the overturning configuration
¹⁹ in our model is whether the Antarctic Intermediate Waters are denser than northern subpolar
²⁰ waters, something that depends on the magnitude and configuration of atmospheric freshwater
²¹ transport. For the modern ocean, we find that although the interbasin atmospheric freshwater flux
²² suppresses Pacific sinking, the poleward atmospheric freshwater flux out of the subtropics enhances
²³ it. When atmospheric temperatures are held fixed, North Pacific overturning can strengthen with
²⁴ either increases or decreases in the hydrological cycle, as well as under reversal of the interbasin
²⁵ freshwater flux. Tipping-point behavior, where small changes in the hydrological cycle may cause
²⁶ the dominant location of densification of light waters to switch between basins and the magnitude
²⁷ of overturning within a basin to exhibit large jumps, is seen in both transient and equilibrium states.
²⁸ This behavior is modulated by parameters such as the poorly constrained lateral diffusive mixing
²⁹ **coefficient**. If hydrological cycle amplitude is varied consistently with global temperature, northern
³⁰ polar amplification is necessary for the Atlantic overturning to collapse. Certain qualitative insights
³¹ incorporated in the model can be validated using a fully-coupled climate model.

32 SIGNIFICANCE STATEMENT: Currently, the global overturning circulation involves conver-
33 sion of [waters lighter than Antarctic Intermediate Water](#) to [deep waters denser than Antarctic](#)
34 [Intermediate Water](#) primarily [light water to dense water](#) in the North Atlantic, rather than [in](#) the
35 North Pacific or [Southern Ocean waters in the](#) Southern Oceans. Many different factors have been
36 invoked to explain this configuration, with atmospheric freshwater transport, basin geometry, lat-
37 eral mixing, and Southern Ocean winds playing major roles. This paper develops a simple theory
38 that combines previous theories, presents the intriguing idea that alternate configurations might be
39 possible, and identifies multiple possible tipping points between these states.

40 1. Introduction

41 The fact that the transformation of light surface waters to dense deep waters is dominated
42 by processes in the North Atlantic basin has profound implications for the ocean's physical and
43 biogeochemical structure (Gnanadesikan 1999; Marinov et al. 2006), as well as for global climate.
44 While some of the cold, dense water that rises to the surface in the Southern Ocean cools further
45 and sinks to form the Antarctic Bottom Water, some of it moves northward and is freshened and
46 warmed as it is transformed into lighter Antarctic Intermediate (AAIW) and Subantarctic Mode
47 Water (SAMW) (Lumpkin and Speer 2007). Additionally, downward diffusion of heat transforms
48 some dense deep water into lighter surface waters. These processes are balanced by a sinking
49 of North Atlantic Deep Water (NADW) in the North Atlantic. This meridionally asymmetric
50 pattern is associated with a cross-equatorial heat transport (Trenberth et al. 2019), so that a given
51 northern latitude is usually several degrees warmer than its southern counterpart. [This asymmetry](#)
52 [in temperatures also helps](#)~~It also help~~ to keep the intertropical convergence zone and associated
53 rainfall north of the equator (Zhang and Delworth 2005).

54 Inverse models constrained with transient tracers (DeVries and Primeau 2011) suggest that fully
55 65% of the water away from the surface mixed layer will first come into contact with the atmosphere
56 within the surface layers of the Southern Ocean. A key driver of the dominance of this region is
57 that the westerly winds within the unblocked latitudes of Drake Passage generate a net northward
58 surface flow of water. As noted by a number of authors (Toggweiler and Samuels 1993, 1995;
59 Gnanadesikan 1999), this water cannot be supplied via a western boundary current carrying light
60 subtropical water poleward along a continental boundary. Instead, it must be upwelled from greater

61 depths. Some fraction of this rising water is supplied by dense water flowing southward below
62 the depth of ridges, while some is supplied by boluses of lighter low-latitude waters associated
63 with mesoscale eddies (Johnson and Bryden 1989; Hallberg and Gnanadesikan 2001; Klinger and
64 Haine 2019).

65 In ocean-only models (Fučkar and Vallis 2007; Johnson et al. 2007; Wolfe and Cessi 2011), the
66 structure of the zonally averaged overturning circulation has been shown to be highly dependent on
67 whether surface fluxes can make the Southern Ocean intermediate waters advected northward at the
68 tip of Drake Passage lighter than NADW. If the nominal NADW becomes lighter than the nominal
69 Antarctic Intermediate Water, then AAIW densities will not outcrop in the Northern Hemisphere.
70 Given the low levels of diapycnal mixing observed away from the mixed layer, in such situations
71 the net watermass transformation in the Southern Ocean must be small. If a steady-state is to be
72 achieved throughout the ocean, the bulk of the northward flux of lighter waters in the Southern
73 Ocean associated with northward Ekman transport must then be balanced by a southward flux of
74 waters of similar density. This flux would be associated with some combination of mesoscale and
75 stationary eddies (Johnson and Bryden 1989; Hallberg and Gnanadesikan 2001).

76 In addition to the north-south asymmetry in the overturning, there is also an interbasin asymmetry,
77 whereby no counterpart to the NADW is formed in the Pacific. In a seminal paper Warren (1983)
78 discussed reasons for this asymmetry, arguing that two factors play an important role in producing
79 a relatively fresh surface. First, he claimed that the **subpolar** North Pacific receives a greater net
80 air-sea flux of freshwater than the **subpolar** North Atlantic. Second, he noted that the relatively
81 weak North Pacific overturning will be much less effective at removing this freshwater than the
82 more vigorous Atlantic overturning. These two mechanisms, asymmetry in freshwater delivery and
83 preferential flushing of the Atlantic, remain the two leading processes discussed in the literature
84 today (Ferreira et al. 2018; Johnson et al. 2019).

85 In idealized coupled models, these two processes work together to localize overturning in the
86 Atlantic. In models with a wide basin (representing the Pacific) and a narrow basin (representing
87 the Atlantic), dense water formation tends to occur preferentially in the narrow basin. **There are**
88 **at least two reasons for this. In idealized energy moisture balance models without a dynamical**
89 **atmosphere (De Boer et al. 2008; Jones and Cessi 2016, 2017; Youngs et al. 2020) Assuming** the
90 atmospheric freshwater transport F_w^{basin} between the subtropical and subpolar gyres scales as the

91 basin width L_x^{nbasin} . In more dynamically sophisticated models such as Ferreira et al. (2010) the
92 mid-latitude storm track penetrates from the short to the long basin but not from the long to the short
93 basin. In both cases the subpolar gyre of a wide basin will receive more freshwater than a narrow
94 basin so that the overturning has to remove more freshwater. If the overturning circulation within that
95 a basin has magnitude M_{basin} , the salinity difference between high and low latitudes within that
96 basin will scale as $\Delta S_{basin} \approx -(F_w^{basin}/M_{basin})S_0$ where S_0 is some average salinity. Thus, given
97 two idealized basins with equivalent initial overturning, the wider basin with a larger freshwater
98 flux $F_w^{wide} > F_w^{narrow}$ will exhibit a larger salinity difference ($\Delta S_{wide} > \Delta S_{narrow}$). But since the
99 impact of this gradient on density is to make polar waters lighter with respect to the tropics, it will
100 produce a weaker poleward density gradient. The weaker gradient will retard the overturning in
101 the wider basin relative to the narrow basin. As less light water is transformed to dense water in
102 the wide basin, the sea surface within the wider basin will stand higher and pump **tropical** water
103 into the narrow basin, **which will in general be saltier than water entering the narrow basin from**
104 **the Southern Ocean**. This interbasin transport **as well as the additional salt that it carries** then
105 reinforces the overturning in the narrow basin **particularly if the eastern boundary of this basin**
106 **does not extend as far to the south** (Nilsson et al. 2013; Jones and Cessi 2017). Note that the
107 **energy-balance** models cited above do not resolve the high topography of the Rockies and Andes
108 (which block the eastward mid-latitude transport of water vapor from the Pacific to the Atlantic)
109 or the east African highlands (which block westward tropical transport of water vapor from the
110 Indian to the Atlantic).

111 Insofar as the hydrological cycle is responsible for localizing of the overturning to the North
112 Atlantic, we would expect Pacific overturning only when conditions are cooler, as the amplitude of
113 the hydrological cycle tends to track global temperatures. However, there are a number of lines of
114 evidence that suggest that this picture may be incomplete. First, both idealized models and realistic
115 coupled models can generate some overturning in the Pacific given modern conditions (De Boer
116 et al. 2010; Bahl et al. 2019). As noted in the latter paper, the overturning is highly sensitive to
117 the lateral diffusion coefficient A_{Redi} associated with mesoscale eddies, whose spatial structure is
118 poorly understood (Abernathy et al. 2022). Second, paleoceanographic evidence suggests that
119 there have been times in the past when there was more deep water formation in the North Pacific
120 (Rae et al. 2014; Burls et al. 2017; Ford et al. 2022), as there is evidence of lower levels of chemicals

produced by the decomposition of organic material. This includes cold periods such as the Younger Dryas when the climate was colder and freshwater transport was presumably weaker than today, both between basins and from the subtropical to subpolar gyres. However it also includes the relatively warm Pliocene, during which the freshwater transports were likely even stronger. Third, although the modern atmosphere does appear to transport less freshwater from the low latitudes to the high latitudes between 40°S and 65°N in the Atlantic relative to the Pacific (as summarized in Ferreira et al. 2018), it also deposits significant freshwater flux in the Arctic. As we will argue below, this re-enters the global ocean in the Atlantic and *reduces* the extent to which the northern subpolar Atlantic is saltier and denser than the subpolar Pacific.

This paper seeks insight into the dynamics of how the configuration and magnitude of the hydrological cycle control the configuration and magnitude of the overturning using a relatively simple dynamical box model. Such approaches have a long history of giving insight into the dynamics and sensitivity of the overturning (Johnson et al. 2019). For example, the pioneering paper of Stommel (1961) showed that the opposing effects of high latitude cooling and poleward atmospheric freshwater transport could combine to produce a bistable overturning describable by two fold bifurcations. Tziperman et al. (1994) showed that this mechanism could also operate in a fully coupled model, but that it only appeared for some initial conditions. Huang et al. (1992) showed the potential existence of multiple steady states when resolving deep and surface boxes in the Northern, low-latitude and Southern oceans. Gnanadesikan (1999) helped to explain how changes in Southern Ocean winds and eddies help determine the magnitude of the northern hemisphere overturning by controlling the transformation of dense water to light water. Johnson et al. (2007) extended the latter model to include prognostic equations for temperature and salinity and showed that, similar to the Stommel model, the balance between the hydrological and heat cycles could produce two stable states of overturning. In this case, the stable state is controlled by the density difference between the North Atlantic Deep Water and Southern Ocean surface waters. If the Southern Ocean surface is sufficiently light, the transformation of dense to light water in the Southern Ocean and low-latitude pycnocline is balanced by overturning in the North with a relatively shallow low-latitude pycnocline. If the Southern Ocean surface is denser than the subpolar North Atlantic, it is balanced by eddy fluxes of [volumemass](#) to the Southern Ocean associated with a deep low-latitude pycnocline. Jones and Cessi (2016) extended the Gnanadesikan

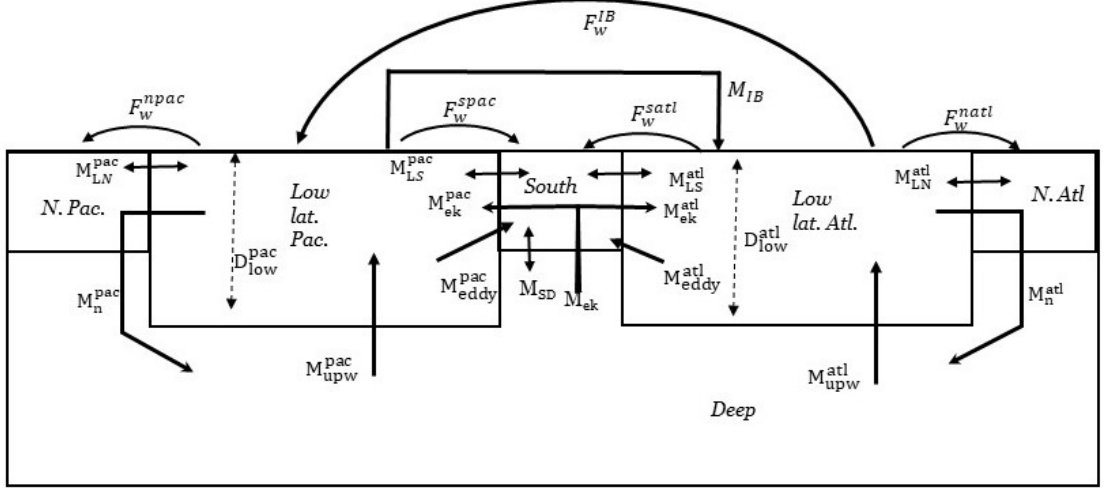
151 (1999) model to include a Pacific basin- explicitly looking at how Southern Ocean winds control
152 the flow of water between the Pacific-Indian and Atlantic basins, arguing that this produced a
153 deeper pycnocline in the Pacific relative to the Atlantic. Gnanadesikan et al. (2018) extended the
154 Johnson et al. (2007) model to include lateral tracer mixing. That paper examined what happened
155 when hydrological fluxes were adjusted to make a model with "incorrect" physics look like a model
156 with "correct" physics. While flux adjustment sometimes produced more realistic estimates of the
157 stability of the overturning when the hydrological cycle amplitude was increased, as suggested by
158 Liu et al. (2017), it did not always do so.

159 In this work we extend the model of Gnanadesikan et al. (2018) to include a separate low-latitude
160 Pacific-Indian ocean box and a high-latitude Pacific box. We include a low-latitude exchange
161 term between the Indo-Pacific and Atlantic similar to that formulated previously (Jones and Cessi
162 2016) thus potentially distinguishing the "warm-water" and "cold-water" pathways by which light
163 water enters the Atlantic basin. The model can also be seen as extending Jones and Cessi (2016)
164 by allowing for prognostic salinity and temperature and for a potential North Pacific overturning.
165 The resulting model exhibits a phenomenologically rich interplay between freshwater fluxes and
166 different regimes of overturning, predicting a number of new "tipping points" between states.

167 2. Model description

168 a. Equations

169 A "wiring diagram" of the model is shown in Figure 1. A full description of the model variables,
170 parameters and equations is provided in the Supplemental Material. The model has two northern
171 latitude boxes, each of which is capable of transforming warm, salty low-latitude water into colder,
172 lower-salinity surface, intermediate, or deep water. The high latitude boxes also exchange water
173 and tracers with low-latitude boxes in each basin. Freshwater fluxes are specified between the
174 low-latitude boxes and the high latitude boxes ($F_w^{npac}, F_w^{natl}, F_w^{spac}, F_w^{satl}$) as well as between the
175 two low-latitude boxes (F_w^{IB}). This allows us to examine the effect of changes in the magnitude
176 of freshwater fluxes such as might be associated with climate change, as well as differences in the
177 configuration of freshwater fluxes (i.e. the ratio of F_w^{npac} to F_w^{IB}), which may vary considerably
178 from one climate model to another.



169 FIG. 1. Schematic of our six box model. Note that the circulation is centered on the Southern Ocean, as in
 170 Lumpkin and Speer (2007).

181 A key aspect of this model is that the pycnocline depth is not a fixed parameter. This contrasts
 182 with the classic box models (Stommel 1961; Rooth 1982; Huang et al. 1992; Tziperman et al.
 183 1994) previously referred to as well as the more recent versions by Alkhayouon et al. (2019),
 184 where the overturning throughout the ocean is directly proportional to density differences between
 185 different regions. The depths of the pycnocline in the Atlantic (D_{low}^{atl}) and Indo-Pacific (D_{low}^{pac})
 186 are state variables whose evolution is predicted by two **volumemass** balance equations which
 187 depend in part on density difference between the northern and southern latitudes. We define
 188 $\rho_{natl,npac,latl,lpac,S,deep}$ as the densities of the North Atlantic, North Pacific, low latitude Atlantic
 189 and low latitude Pacific/Indian, Southern Ocean surface and deep ocean respectively. Then letting
 190 $Area_{latl,lpac}$ be the area of the low-latitude Atlantic and Pacific/Indian boxes, we can define

$$Area_{latl} \frac{\partial D_{low}^{atl}}{\partial t} = M_{ek}^{atl} + M_{upw}^{atl} - M_{eddy}^{atl} - M_n^{atl} (\rho_{natl} > \rho_{latl}, \rho_S) + M_{IB} - F_w^{satl} - F_w^{natl} - F_w^{IB}, \quad (1)$$

$$Area_{lpac} \frac{\partial D_{low}^{pac}}{\partial t} = M_{ek}^{pac} + M_{upw}^{pac} - M_{eddy}^{pac} - M_n^{pac} (\rho_{npac} > \rho_{lpac}, \rho_S) - M_{IB} - F_w^{spac} - F_w^{npac} + F_w^{IB}, \quad (2)$$

where the M_{ek} fluxes represent the upwelling of dense water into the Southern Ocean mixed layer and its subsequent export into the mid-latitude pycnocline; the M_{eddy} fluxes represent the supply of light water to the Southern Ocean driven by eddy thickness fluxes; the M_{upw} terms represent diffusive upwelling in the pycnocline; and M_{IB} represents the exchange of **volumemass** between the basins. Terms of the form $\rho_A > \rho_B$ are set to 1 if true and zero if false. We note that the northern overturning only changes the volume of the low-latitude box if the high-latitude box is *denser than that of the corresponding low-latitude and Southern Hemisphere surface boxes*. If it is not, the assumption is that the water entering the high latitude box will return to the low-latitude box.

As in previous work (Gnanadesikan 1999; Gnanadesikan et al. 2018) the model describes the water fluxes between the boxes in terms of parameters and state variables. Following Gnanadesikan (1999) and Gnanadesikan et al. (2018) the overturning fluxes in each basin M_n^{atl} and M_n^{pac} are taken as proportional to the depth-integrated geopotential difference, which is tightly coupled to the available potential energy. Such a relationship has been found to hold in models (Bryan 1987; De Boer et al. 2010; Levermann and Fürst 2010) and in laboratory experiments (Park and Whitehead 1999). ~~The basic idea behind this is that the overturning velocity at a given depth is proportional to the meridional pressure gradient $v \propto -\frac{1}{\rho} \frac{\partial p}{\partial y}$~~ In Bryan (1987) this arises from assuming that the vertical shear associated with the overturning is proportional to the thermal wind shear ~~overturning velocity is some fraction of the eastward geostrophic velocity~~

$$\frac{\partial v}{\partial z} = C_0 * \frac{\partial u}{\partial z} = C_0 * \frac{g \Delta \rho(z)}{\rho f L_y^n} \quad (3)$$

where f is the Coriolis parameter and L_y^n is the meridional scale over which the pycnocline shallows in the north) ~~and $\Delta \rho(z)$ is an averaged meridional density difference at a given depth and integrating this in the vertical from a level of no motion~~. When we integrate over the width of the current L_y^n drops out and the horizontally-integrated velocity **shear** at a given depth becomes

$$\int \frac{\partial v}{\partial z} dy = C_0 \frac{g \Delta \rho(z)}{\rho f} \quad (4)$$

214 In Gnanadesikan (1999) the overturning velocity is related to the frictional balance in the western
 215 boundary current

$$v = -C_1 * \frac{L_B^2}{A_H} \frac{\Delta p}{\rho L_y^n} \quad (5)$$

216 which again implies that that

$$\frac{\partial v}{\partial z} = C_1 * \frac{L_B^2}{A_H} \frac{g * \Delta \rho(z)}{\rho L_y^n} \quad (6)$$

217 where $L_B = (A_H/\beta)^{1/3}$ is the thickness of the boundary layer, A_H is the lateral eddy viscosity,
 218 and $\beta = \partial f / \partial y$. Note that in this case there is an implicit assumption that $\Delta \rho(z)$ in the boundary
 219 current mirrors that in the basin as a whole.

220 When we double integrate (4) over depth we get that the overturning scales as.

$$M_n = \frac{g * \Delta \rho}{\rho \epsilon} * D^2 \quad (7)$$

221 where $\Delta \rho$ is an averaged density difference and D is the pycnocline depth. In this formulation, ϵ
 222 represents a resistance parameter

$$\epsilon = \left(\frac{C_0}{f} \int_{z=-z_0}^0 \int_{z'=-z_0}^z \Delta \rho(z) / \Delta \rho * (dz'/D) * (dz/D) \right)^{-1} \quad (8)$$

223 Similarly, if we integrate (6) integrated over the boundary layer the eddy viscosity drops out. If
 224 we then double-integrate with depth we get a functionally equivalent equation to (8), with C_0/f
 225 replaced with $C_1/\beta L_y^n$. transport at a given depth becomes proportional to $g \Delta \rho / \rho \beta L_y^n$, though C in
 226 (6) will not be the same as in (3).

227 Both approaches assume that we can find the relevant pressure by integrating. Given that from the
 228 hydrostatic equation $\Delta p(z) = - \int_{z'=z_0}^z g * \Delta \rho(z') dz'$ where z_0 is a level of no motion, we can integrate
 229 in the vertical to get the transport $M_{over} = C \int_{z=z_0}^0 \left(\int_{z'=z_0}^z \frac{g * \Delta \rho(z')}{\rho} dz' \right) dz$. If we nondimensionalize
 230 the density by $\Delta \rho$ and the depth by D , this depth integrated velocity will be proportional to
 231 $M_n \propto g \Delta \rho D^2 / \rho$ where the constant of proportionality, which as in previous work we define as $1/\epsilon$,

232 Note that ϵ incorporates the relationship between the pycnocline depth D and the level of no
 233 motion z_0 , the functional dependence of the meridional density gradient on depth and the small
 234 scale physics of the models (incorporated in the constants C_0, C_1) that allow for ageostrophic

235 overturning. Using the definition of D discussed in Gnanadesikan (1999), if we assume that the
 236 pycnocline can be represented by a single jump in density at the level of no motion z_0 , then the
 237 pycnocline depth $D = z_0/2$ and the integrated thermal wind shear will be $M_{thermal} = (2g\Delta\rho D^2)/\rho f$.
 238 If instead the density anomaly drops linearly to the level of no motion z_0 , then $D = z_0/3$ and
 239 $M_{thermal} = (3g\Delta\rho D^2)/2\rho f$. Insofar as $M_{over} = C_0 * M_{thermal}$, in the first case $\epsilon = f/2C_0$, while in
 240 the second $\epsilon = 2f/3C_0$. Note also that our formulation here makes the overturning proportional to
 241 the available potential energy.

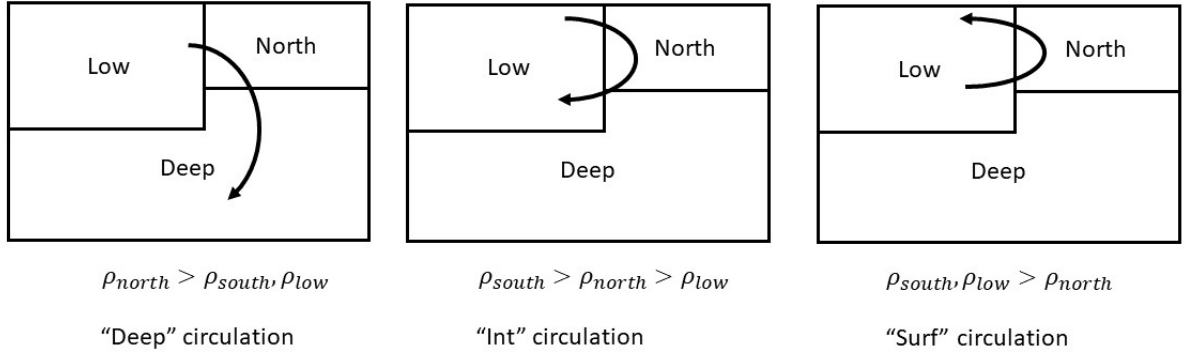
242 More specifically for our model we write

$$M_n^{atl,pac} = \frac{g(\rho_{natl,npac} - \rho_{latl,lpac})D_{low}^{atl,pac}^2}{\rho_{natl,npac}\epsilon_{natl,npac}}. \quad (9)$$

253 where the density is computed using the full nonlinear equation of state using the temperature and
 254 salinity within the boxes with pressure referenced to the surface.

255 We note that this formulation then produces multiple possible configurations for the overturning
 256 circulation in each basin, outlined schematically in Fig. 2. When the northern basin is denser
 257 than either the low latitude or the Southern Ocean box it forms deep water. We refer to this as a
 258 "DA" circulation when it is found in the Atlantic and a "DP" circulation when it is found in the
 259 Pacific. When the northern basin has a density between that of the Southern Ocean and that of the
 260 low-latitudes (as is the case for the Pacific today), we consider it as forming intermediate water
 261 (and refer to it as "IA" and "IP" for the Atlantic and Pacific respectively). When the northern basin
 262 becomes sufficiently fresh, as in the "off" state of the Stommel (1961) model, low-latitude water
 263 flows into the basin, gets lighter and is returned to the tropics. We refer to this situation as an "SA"
 264 or "SP" circulation for the Atlantic and Pacific respectively. Note that the designation refers to the
 265 *configuration in density space* of the pathways involved, and not necessarily to the *magnitude* of
 266 the pathways. Note also that these configurations will imply different relationships between z_0 and
 267 D_{low} , which as noted previously would be expected to affect ϵ .

268 We can then combine these designations to define a taxonomy of the Northern Hemisphere
 269 overturning. The modern ocean would then be described as "DA-IP", while an ocean in which the
 270 freshwater flux is strong enough to produce freshwater caps in both the North Atlantic and Pacific
 271 would be described as a "SA-SP" ocean. The circulation during the Last Glacial Maximum was



243 FIG. 2. Schematic of flows associated with different relationships between density in the southern, low-
 244 latitude and northern surface boxes. "Deep" circulation involves formation of water in the northern basin that is
 245 denser than both the Southern Ocean and the low-latitude surface boxes and thus is able to connect to the deep.
 246 Dynamically it is characterized by a positive overturning circulation as well as lower resistance ϵ to overturning.
 247 "Intermediate" circulation involves formation of water in the northern basin that is lighter than the Southern
 248 Ocean water but heavier than the tropics in that basin, similar to what we find in the Pacific today. Dynamically
 249 it is characterized by positive values of overturning but with higher resistance ϵ . "Surface" circulation involves
 250 low-latitude water entering the high latitudes and becoming lighter there- similar to what happens in the Arctic or
 251 Baltic today. For Northern Basins, this occurs when the density is lighter than both the low-latitude and Southern
 252 Ocean boxes. Dynamically it is characterized by negative values of overturning.

252 arguably an "IA-IP" circulation. (Rafter et al. 2022). This taxonomy will become relevant as we
 273 discuss solutions of the model in the Results section.

274 Following Gnanadesikan (1999) we allow for diffusive closures of the M_{eddy} and M_{upw} terms

$$M_{eddy}^{atl,pac} = \frac{A_{GM} D_{low}^{atl,pac} L_x^{satl,spac}}{L_y^s}, \quad (10)$$

$$M_{upw}^{atl,pac} = \frac{K_v Area_{latl,lpac}}{D_{low}^{atl,pac}}, \quad (11)$$

275 where A_{GM} is a thickness diffusion coefficient following (Gent and Mcwilliams 1990), K_v is a
 276 vertical diffusion coefficient, the L_x terms are the length of the Southern boundary of each basin,
 277 and L_y^s is the length scale over which the pycnocline shallows in the south. Note that Levermann
 278 and Fürst (2010) found that in realistic climate models the effective length scale L_y^s may depend

279 on local density gradients, a process not included in the present study. Similarly we can define the
 280 Ekman flux as

$$M_{ek} = \int_s \vec{\tau} * d\vec{s} / \rho f \quad (12)$$

281 where s describes some closed pathway around the Southern Ocean. There has been some
 282 discussion in the literature about how this pathway should be chosen. Gnanadesikan (1999)
 283 defined it as the northernmost latitude circle unblocked by a continent, which for the ECMWF
 284 wind produce yields a flux of 28.5 Sv. However, Allison et al. (2010) argued that within idealized
 285 models averaging the transport over the ACC yielded a better prediction. Depending on which
 286 wind product is used and where one chooses the bounds of integration, one can find values ranging
 287 from 20-35 Sv. Our value of 24 Sv lies towards the lower edge of this range.

288 The exchange term is modified from Jones and Cessi (2016) as

$$M_{IB} = \frac{g [(\rho_{deep}/\rho_{lpac} - 1)D_{low}^{pac} - (\rho_{deep}/\rho_{latl} - 1)D_{low}^{atl}]}{\epsilon_{IB}} \min(D_{low}^{pac}, D_{low}^{atl}) \quad (13)$$

289 so that it is proportional to the pressure difference between the two basins integrated over the
 290 minimum of the pycnocline depths. Note that this is slightly different than the original Jones
 291 and Cessi (2016) formulation, which turns out to be numerically unstable when the densities are
 292 allowed to vary separately in the two basins. Thus having an Indo-Pacific basin that is lighter than
 293 the Atlantic (as is the case in real life) allows for a circulation from the Indo-Pacific to the Atlantic.
 294 We do not consider in this paper the effects of wind stress curl in modulating the pressure gradient
 295 at the boundary between the Indian and Pacific Oceans as in Jones and Cessi (2016), but this
 296 represents a relatively straightforward future extension. It is worth noting, however, that in order
 297 to highlight the importance of these winds, Jones and Cessi (2016) assumed the density contrast
 298 between light and dense waters to be fixed (as was also the case in Gnanadesikan (1999)). For now
 299 the effect of the winds should be thought of as being implicitly included in ϵ_{IB} .

300 In this paper we also allow the temperatures and salinities to be determined by prognostic
 301 equations as in the single basin overturning models of Johnson et al. (2007) and Gnanadesikan
 302 et al. (2018). In addition to the **volumemass** fluxes already described, the resulting balance
 303 equations also allow for terms due to lateral tracer stirring (Redi 1982), which produces mixing

304 fluxes between low and high latitude boxes of the general form

$$M_{LN,LS}^{atl,pac} = \frac{A_{Redi} D_{low}^{atl,pac} L_x^{natl,npac,satl,spac}}{L_y^{natl,npac,satl,spac}}, \quad (14)$$

305 This mixing flux then produces transports of the form $M_{LN,LS}^{atl,pac,S} = (T_{latl,lpac} - T_{natl,npac,S})$ for
 306 temperature and $M_{LN,LS}^{atl,pac} = (S_{latl,lpac} - S_{natl,npac,S})$ for salinity.

307 We also allow for a mixing flux M_{SD} in the Southern Ocean that simulates the impact of bottom
 308 water formation/mixing of intermediate water into the deep. This flux is held constant in all the
 309 simulations described in this paper. It allows salt added to the Southern Ocean to escape to the
 310 deep ocean rather than being necessarily injected into the low-latitude pycnocline.

311 Finally, heat exchange between each surface box and the overlying atmosphere is handled using
 312 a restoring equation of the form

$$\frac{\partial}{\partial t} (D_X * T_X) = D_{mix}/\tau_{rest} * (T_X^{atm} - T_X) \quad (15)$$

315 Note that this means that the high latitude boxes (for which $D_X = D_{mix}$ are more tightly tied to the
 316 atmospheric temperature than are the low-latitude boxes. A full list of all the parameters is given
 317 in Table 1.

318 *b. Calibrating the model*

323 In Gnanadesikan et al. (2018) we calibrated the parameters governing the overturning in the
 324 northern hemisphere based on what is known about the rate of overturning and mean watermass
 325 properties. As in previous work, we calculate the observed pycnocline depth using data from the
 326 World Ocean Atlas 2013 (Locarnini et al. 2013; Zweng et al. 2013) as

$$D = \frac{\int_{z=-2000}^0 z(\sigma_1(z) - \sigma_1(z=2000)) dz}{\int_{z=-2000}^0 (\sigma_1(z) - \sigma_1(z=2000)) dz} \quad (16)$$

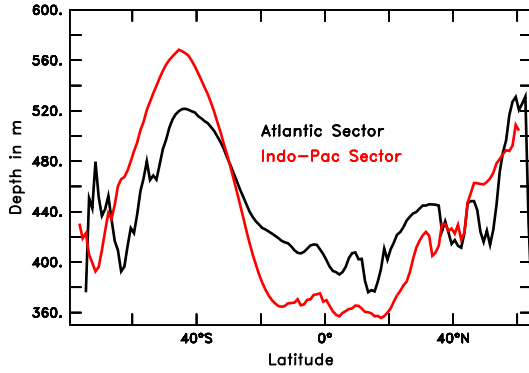
327 which for an exponential profile gives the e-folding depth. As shown in Fig. 3a, the exact value
 328 of the horizontal averaged $D_{low}^{atl,pac}$ that we use as a model variable will depend sensitively on the
 329 exact bounds of integration. Choosing the range 30°S to 45°N in the Atlantic and 30°S to 40°N in

313 TABLE 1. List of key parameters used in the model. Values that are varied from the control are shown in bold
 314 with alternatives shown in italics

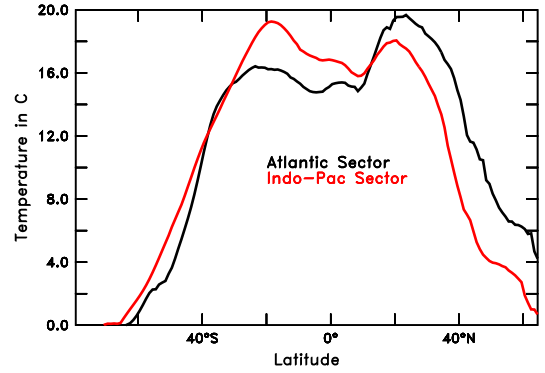
Parameter	Description	Values
$Area_{ocean}$	Area of the ocean	$3.6 \times 10^{14} \text{ m}^2$
$Area_{latl}$	Area of the low latitude Atlantic	$0.64 \times 10^{14} \text{ m}^2$
$Area_{lpac}$	Area of the low latitude IndoPacific	$1.98 \times 10^{14} \text{ m}^2$
$Area_{s}$	Area of the Southern Ocean	$0.62 \times 10^{14} \text{ m}^2$
$Area_{natl}$	Area of the N.Atl+Arctic	$0.22 \times 10^{14} \text{ m}^2$
$Area_{npac}$	Area of the North Pacific	$0.1 \times 10^{14} \text{ m}^2$
L_x^{satl}	Length of Southern boundary of low-latitude Atlantic.	$6.25 \times 10^6 \text{ m}$
L_x^{spac}	Length of southern boundary of low-latitude IndoPacific.	$18.75 \times 10^6 \text{ m}$
L_x^{natl}	Length of northern boundary of low-latitude Atlantic	$5 \times 10^6 \text{ m}$
L_x^{npac}	Length of northern boundary of low-latitude Pacific (m)	$10 \times 10^6 \text{ m}$
$L_y^{satl,spac,natl,npac}$	Length over which pycnocline shallows	$1 \times 10^6 \text{ m}$
D_{oc}	Depth of ocean	3680 m
D_{mix}	Depth of High Latitude surface layers	100 m
K_v	Vertical diffusion coefficient	$1 \times 10^{-5} \text{ m}^2 \text{s}^{-1}$
M_{ek}^{atl}	Ekman flux in the Atlantic	6 Sv
M_{ek}^{pac}	Ekman flux in the Pacific	18 Sv
AGM	Thickness diffusion coefficient	$1000 \text{ m}^2 \text{s}^{-1}$
A_{Redi}	Tracer diffusion coefficient	1000, 400, 2400 $\text{m}^2 \text{s}^{-1}$
$\epsilon_{natl0,npac0}$	Baseline resistance to overturning	$1.4 \times 10^{-4} \text{ s}^{-1}$
$\Delta\rho_{trans}$	Width of transition over which resistance increases	0.1 kg m^{-3}
ϵ_{IB}	Resistance to interbasin flow	$0.7 \times 10^{-4} \text{ s}^{-1}$
F_w^{natl}	Baseline freshwater transport from low-latitude to N. Atl.	0.45 Sv
F_w^{npac}	Baseline freshwater transport from low-latitude to N. Pac.	0.34 Sv, 0.6 Sv
F_w^{satl}	Baseline freshwater transport from low-latitude Atl. to SO	0.275 Sv
F_w^{spac}	Baseline freshwater transport from low-latitude Pac to SO	0.825 Sv
F_w^{IB}	Baseline interbasin flux	0.15 Sv
M_{SD}	Mixing between Southern surface and deep	15 Sv
$T_{natl,npac,latl,lpac,SO}^{atm}$	Baseline atmospheric restoring temperatures	0.3, 1.3, 16.8, 18.2, 2.8 $^{\circ}\text{C}$
τ_{rest}	Restoring time for temperatures	1 yr

330 the IndoPacific (reflecting the differences in the northward drift of the North Atlantic current vs.
 331 the Kuroshio) gives us pycnocline depths of 420m in the Atlantic and 380m in the Pacific.

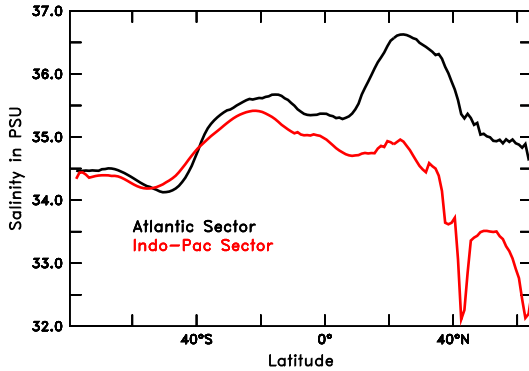
332 Beginning with the Southern Ocean, we have a target mean salinity of around 34 PSU and
 333 temperature of around 4 $^{\circ}\text{C}$ for the Antarctic Intermediate Waters. Given that modern deep waters
 334 are roughly equally fed from the south and the north, we set M_{SD} to 15 Sv. When we add up all the
 335 salt fluxes entering and leaving the Southern Ocean surface box, we find that we need a freshwater



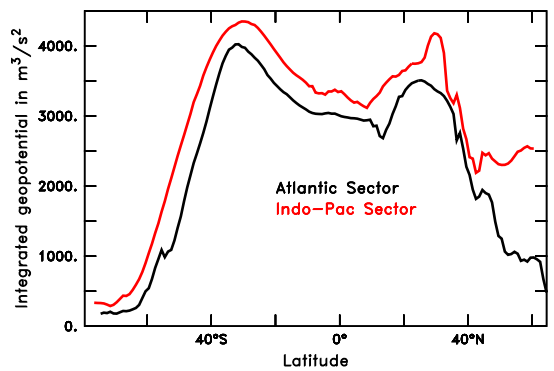
(A) Pycnocline Depth



(B) Upper Ocean Temperature (0–400m)



(C) Upper Ocean Salinity (0–400m)



(D) $g'(\Delta\rho/\rho)z_{\text{pyc}}^2$ ($\text{m}^3 \text{ s}^{-1}$)

319 FIG. 3. Zonally averaged structure of upper ocean hydrography computed from World Ocean Atlas 2013
 320 (Locarnini et al. 2013; Zweng et al. 2013). Black and red lines show values averaged over the Atlantic and
 321 IndoPacific respectively. (a) Pycnocline depth; (b) Upper ocean temperature; (c) Upper-ocean salinity; (d) Upper
 322 ocean $g'D_{\text{pyc}}^2$.

336 flux of about 1.1 Sv to balance them. While this value is close to the 1.04 Sv found by Tsukernik
 337 and Lynch (2013) using the ECMWF reanalysis, we note that such reanalyses are quite uncertain
 338 (Yu et al. 2017). We divide the Southern Ocean into an Atlantic sector whose southern boundary
 339 comprises 25% of the total length of the northern edge of the Southern Ocean ($L_x^{\text{satl}} = 6.25 \times 10^6 \text{ m}$)
 340 and let the IndoPacific comprise the rest of the boundary ($L_x^{\text{spac}} = 1.875 \times 10^6 \text{ m}$). We set the

341 freshwater flux to the Southern Ocean in our baseline case to mirror this partitioning, so that
342 $F_w^{satl} = 1.1Sv * 0.25 = 0.275Sv$ and $F_w^{spac} = 1.1Sv * 0.75 = 0.825Sv$.

343 We then turn to the Atlantic. The mean temperature and salinity above the pycnocline in the
344 low-latitude Atlantic are 16.2°C and 35.8 PSU respectively in the 2013 World Ocean Atlas. We
345 want our northern box to produce deep waters analogous to those found between 800 and 3000m
346 at longitudes within the Atlantic from $45\text{--}50^{\circ}\text{N}$, giving us mean $T \approx 4^{\circ}\text{C}$ and mean $S \approx 35$ PSU.
347 The integrated geopotential difference $g'D^2$ (roughly proportional to APE and shown in Fig. 3d)
348 gives a difference of around $2500 \text{ m}^3 \text{ s}^{-2}$. This is roughly consistent with what is seen when we
349 calculate differences latitude by latitude. Given an overturning of 16-20 Sv, this would give us a
350 value of $\epsilon_{natl} = 1.235 - 1.545 \times 10^{-4} \text{ s}^{-1}$. For our baseline run we let $\epsilon_{natl} = 1.4 \times 10^{-4} \text{ s}^{-1}$. Taking
351 a baseline value of $A_{Redi} = 1000 \text{ m}^2 \text{ s}^{-1}$, the mixing flux computed from (14) is 2 Sv, so that the
352 freshwater flux required to match the observed salinity difference is 0.45 Sv.

353 In the North Pacific, we assume that the there is no deep water formation and so the relevant
354 **volumemass** flux is the formation rate of North Pacific Intermediate Water, with a rough transport
355 of about 6 Sv (Talley 1997; Lumpkin and Speer 2007). Given a low-latitude pycnocline depth of
356 around 380m the low-latitude temperatures and salinities above the pycnocline are 17.2°C and 35
357 PSU respectively. The subpolar waters below the seasonal mixed layer (reflecting North Pacific
358 Intermediate water) have an average temperature of 5.2°C and salinity of 33.8 PSU. This then
359 produces a integrated geopotential difference of $1700 \text{ m}^3 \text{ s}^{-2}$, resulting in a value of $\epsilon_{npac} =$
360 $2.8 \times 10^{-4} \text{ s}^{-1}$, about twice that in the North Atlantic. Allowing for an additional mixing flux of
361 4 Sv due to the wider basin, this gives us a freshwater flux of 0.34 Sv. Note that this flux is
362 actually smaller than in the North Atlantic despite the greater width of this basin. **This undermines**
363 **, undermining** the assumption made in idealized models that it is **a larger freshwater flux to the**
364 **subpolar gyre in the Pacific relative to the subpolar gyre in the Atlantic****the meridional atmospheric**
365 **flux of freshwater** that localizes the overturning to the Atlantic.

366 The difference in the efficiency of overturning between the two basins reflects the difference in
367 flow configuration induced by differences in density. A key difference between the North Atlantic
368 Deep Water and North Pacific Intermediate Water is that the density of the former ($\sigma_{\theta} = 27.8$) is
369 much heavier than the latter ($\sigma_{\theta} = 26.7$). The Antarctic Intermediate Water density ($\sigma_{\theta} = 27.0$) lies
370 between the two. This means that the overturning generated by the near-surface APE difference

371 in the Atlantic has a deeper level of **of** no motion, implying that it receives an extra "kick" from
 372 Antarctic Intermediate water. This results in a smaller ϵ_{natl} . By contrast, in the Pacific, the Antarctic
 373 Intermediate Water slows the overturning, resulting in a larger value of ϵ_{npac} . Rather than focus on
 374 directly representing the dynamics of the intermediate water here, we instead represent this effect
 375 in our model as a transition between low resistance when the northern basin is denser than the
 376 south to a higher resistance when it is lighter.

$$\epsilon_{natl,npac} = 1.4 \times 10^{-4} \left[1.5 + 0.5 \tanh \left(\frac{\rho_{natl,npac} - \rho_s}{\Delta \rho_{trans}} \right) \right]. \quad (17)$$

377 For now, we set $\Delta \rho_{trans} = 0.1 \text{ kg m}^{-3}$, which allows for the configuration we want in the modern
 378 ocean. In the absence of observational evidence for an additional transition when the North Pacific
 379 becomes lighter than the tropical Pacific we do not include a further transition in resistance in this
 380 paper. However, we recognize that further investigation as in Fučkar and Vallis (2007) is warranted.

381 Finally, the interbasin exchange can be gotten by comparing the integrated geopotential difference
 382 relative to the deep water in the two basins. We find that this is around $950 \text{ m}^3 \text{ s}^{-2}$. Given
 383 an interbasin transport of around 13 Sv (Lumpkin and Speer 2007), this implies a resistance
 384 $\epsilon_{IB} = 7 \times 10^{-4} \text{ s}^{-1}$. This resistance is similar to the Coriolis parameter at the Southern tip of Africa,
 385 as would be expected from Jones and Cessi (2016). However, as previously noted it may also
 386 reflect the effect of wind stress curl in deepening the pycnocline as discussed in this paper. If this
 387 were the only process contributing to the contrast between the basins, the interbasin freshwater flux
 388 could then be backed out from this transport and the interbasin salinity difference of 0.8 PSU as
 389 0.3 Sv. However, the fact that the Atlantic and IndoPacific receive different amounts of relatively
 390 fresh Southern Ocean **surface** and deep water also contributes to the interbasin difference, and we
 391 find a better fit in our model with a baseline value of 0.15 Sv. A full set of the relevant freshwater
 392 fluxes is shown in Table 1.

397 Using these baseline parameters we then vary our restoring temperatures in the surface layers
 398 to produce a solution that roughly agrees with the target observations. As shown in Table 2,
 399 the temperatures, salinities, densities, and transports in this solution do not diverge wildly from
 400 our target values. We also present results from a counterfactual simulation in which the baseline
 401 $F_w^{npac} = 0.6 \text{ Sv}$. This configuration results in a DA-SP circulation regime-with a negative overturning

393 TABLE 2. Target values (left-hand column) and final circulation for two versions of the box model. Control
 394 (center column) has a freshwater flux in the North Pacific F_w^{npac} of 0.34 Sv, smaller than the $F_w^{natl} = 0.45Sv$.
 395 Counterfactual case (right-hand column) sets F_w^{npac} to 0.6 Sv, higher than in the North Atlantic, and consistent
 396 with what is often found in idealized models

Parameter	Observed	Control	Counterfactual
N. Atl. T,S (°C,PSU)	4.0, 35.0	4.00,35.06	3.98,35.11
LL. Atl. T,S (°C,PSU)	16.2,35.8	16.21,35.81	16.21,35.86
D_{low}^{atl} (m)	420	429.4	427.9
M_n^{atl} (Sv)	16-20	19.0	18.9
N. Pac T,S (°C,PSU)	5.2,33.8	5.19,33.83	3.67,31.56
LL. Pac. T,S(°C,PSU)	17.2,35.0	17.20,34.95	17.28,35.02
D_{low}^{pac} (m)	380	381.4	378.1
M_n^{pac} (Sv)	2-8	6.4	-1.7
M_{IB} (Sv)	11-15	15.1	14.9
SO T,S (°C,PSU)	4.0,34	4.08,34.09	4.07,34.10
Deep T,S(°C,PSU)	4,34.5	4.03,34.5	4.02,34.50

402 in the North Pacific, indicative of warm salty water being converted to light surface waters, and
 403 a very fresh and cold surface North Pacific. However, changes in the other basins are relatively
 404 small.

405 *c. Numerical Continuation*

406 In the context of studying the proposed six-box overturning circulation model, continuation
 407 algorithms for numerical bifurcation analysis play a crucial role in identifying tipping points.
 408 Specifically, these methods help in analyzing the behavior of the overturning circulation as it
 409 undergoes a “hard” bifurcation, such as a saddle-node/[-a](#)limit point, or a *subcritical* Hopf bifurca-
 410 tion. The present discussion focuses on continuation past limit points ([saddle-node bifurcations](#)),
 411 without aiming to provide a comprehensive guide to all bifurcation scenarios, for which one can
 412 refer to a number of published studies (Dhooge et al. 2008; Doedel 2007; Doedel and Tuckerman
 413 2012; Fabiani et al. 2021).

414 Consider a parameter-dependent dynamical system, described by a system of *autonomous* ordi-
 415 nary differential equations (ODEs)

$$\frac{dy}{dt} = \mathbf{f}(\mathbf{y}; \lambda), \quad f : \mathbb{R}^{n+1} \rightarrow \mathbb{R}^n \quad (18)$$

416 where $\mathbf{y} \in \mathbb{R}^n$ is the n -dimensional state variable vector, $\lambda \in \mathbb{R}$ is a scalar parameter and the function
 417 \mathbf{f} is time-independent and sufficiently smooth. The goal is to construct a *solution curve* Γ for the
 418 system of nonlinear algebraic equations:

$$\Gamma := \{(\mathbf{y}; \lambda) \in \mathbb{R}^{n+1} \text{ such that } \mathbf{f}(\mathbf{y}, \lambda) = 0\}, \quad (19)$$

419 corresponding to the equilibria of the system (18) for various values of the parameter λ . The main
 420 concept underlying numerical continuation methods (Allgower and Georg 2012) is to generate a
 421 sequence of pairs $(\mathbf{y}_i, \lambda_i)$, $i = 1, 2, \dots$ that approximate a specific branch of steady-states, satisfying
 422 a chosen tolerance criterion ($\|\mathbf{f}(\mathbf{y}_i; \lambda_i)\| \leq tol$ for some small $tol > 0$) and involves a *predictor-*
 423 *corrector* process. We start from a known point on the curve, $(\mathbf{y}_i; \lambda_i) \in \Gamma$, and the tangent vector
 424 \mathbf{v}_i to the curve there, computed through the implicit function theorem. To compute a new point
 425 $(\mathbf{y}_{i+1}; \lambda_{i+1})$ we need two steps: (a) finding an initial guess for $(\mathbf{y}_{i+1}, \lambda_{i+1})$ and (b) iteratively
 426 refining the guess to converge towards a point on the curve Γ (19). We denote the initial guess for
 427 $\mathbf{x}_{i+1} \equiv (\mathbf{y}_{i+1}, \lambda_{i+1})$ as $X_{i+1}^{(0)}$, given by:

$$X_{i+1}^{(0)} = \mathbf{x}_i + h\mathbf{v}_i, \quad (20)$$

428 where h is a chosen step size. For a small enough h the prediction $X_{i+1}^{(0)}$ is close to the solution curve
 429 and can be corrected via e.g. a Newton-like scheme. Beyond critical points, where the Jacobian
 430 matrix becomes singular, solution branches can be traced with the aid of numerical bifurcation
 431 theory. For example, solution branches past saddle-node bifurcations (limit points) can be traced by
 432 applying the so called pseudo arc-length continuation method. This involves the parametrization
 433 of both \mathbf{y} and λ by the arc-length s on the solution curve. The solution is sought in terms of both
 434 $\mathbf{y}(s)$ and $\lambda(s)$ in an iterative manner, by solving until convergence an augmented system, involving
 435 eq. (19) and the following pseudo arc-length condition:

$$N(X_{i+1}^{(k)}) = (X_{i+1}^{(k)}(s) - X_{i+1}^{(0)})^T \cdot \mathbf{v}_i = 0. \quad (21)$$

436 The tangent vector v_{i+1} to the curve at the new point is then computed. The direction along the
437 curve must be preserved, i.e. $v_i^T v_{i+1} = 1$, and v_{i+1} must be normalized. Here, to construct the
438 bifurcation diagrams of the 6-box model, we have employed Cl_Matcont version 5.4. Cl_MatCont
439 (Dhooge et al. 2008) is a user-friendly Matlab package that relies on a collection of routines for
440 numerical bifurcation analysis. Continuation codes such as the ones we are using here are capable
441 of detecting certain types of bifurcations (for cases where eigenvalues go from real and negative to
442 real and positive). However, in the case of global bifurcations, where limit points intersect stable
443 orbits, it may be more difficult to classify the bifurcation unambiguously. We therefore only label
444 the cases where an unambiguous bifurcation is detected.

445 *d. Coupled model*

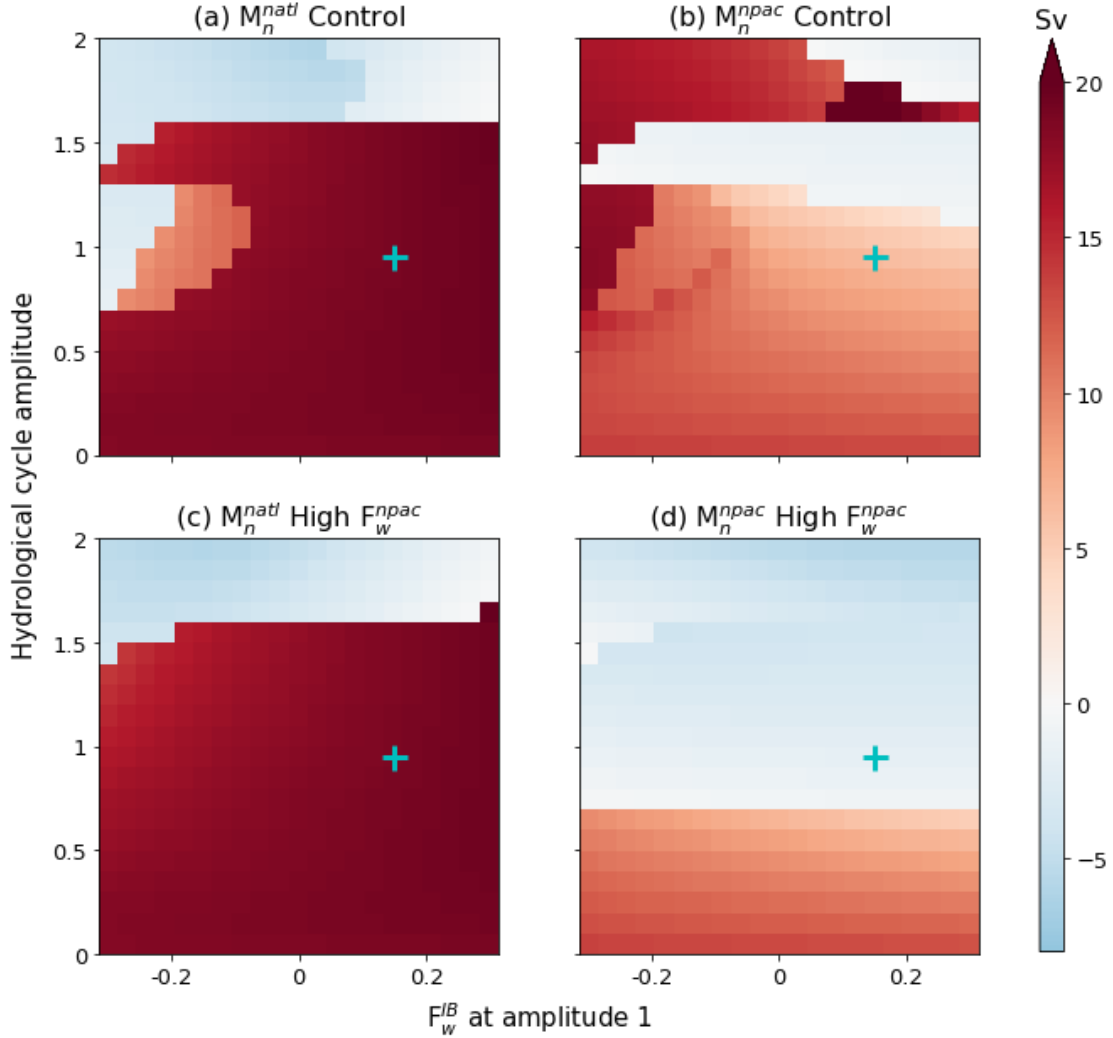
446 A full comparison between the box model and a coupled model is beyond the scope of this
447 manuscript. However, we do use a subset of previously published simulations to show that certain
448 key assumptions used in constructing our box model may also hold in more complex models. The
449 model used is a coarse-resolution version of the GFDL CM2M model, denoted CM2Mc, which
450 contains fully dynamic atmosphere, ocean, ocean biogeochemical, and sea ice components. The
451 baseline simulation is described in Galbraith et al. (2011), to which the reader is referred for a more
452 complete description. In a series of papers, the Gnanadesikan group (Pradal and Gnanadesikan
453 2014; Gnanadesikan et al. 2015; Bahl et al. 2019; Ragen et al. 2022) has explored the impact
454 of changing the lateral mixing coefficient A_{Redi} , which diffuses tracers horizontally within the
455 mixed layer and along isopycnals within the ocean interior. A baseline case with $A_{Redi} = 800$
456 $\text{m}^2 \text{s}^{-1}$ was initialized with modern ocean temperatures and salinities and spun up for 1500 years
457 using preindustrial concentrations of greenhouse gasses. At that point, as described in Pradal and
458 Gnanadesikan (2014), a suite of simulations with a range comparable to those in those in the CMIP5
459 models was branched off the control and run for 1000 model years. At 360 years after this branch,
460 as described in Bahl et al. (2019), additional simulations in which CO_2 was abruptly doubled were
461 initialized from each branch and run for 140 years. In this paper we consider model solutions with
462 $A_{Redi} = 400 \text{ m}^2 \text{s}^{-1}$ (referred to as AREDI400) and $A_{Redi} = 2400 \text{ m}^2 \text{s}^{-1}$ (referred to as ARED2400)
463 for both control and 2x CO_2 cases. 100-year averages from the end of the simulation are used in
464 each case.

465 **3. Results**

466 *a. Interbasin transport and the sensitivity of the overturning configuration to changes in hydrolog-
467 ical amplitude*

468 We begin by examining the interplay between the configuration of the hydrological cycle and the
469 sensitivity of the overturning to instantaneous changes in the amplitude of hydrological cycling.
470 Such changes might be found in an idealized climate model experiment where the greenhouse gas
471 concentrations are suddenly raised or lowered. Starting with our target initial conditions, we define
472 a set of freshwater flux patterns using the inferred $F_w^{natl,npac,satl,spac} = 0.45, 0.34, 0.275$ and 0.825
473 Sv, respectively, but allow the interbasin transport to vary from -0.3 Sv to $+0.3$ Sv (horizontal axes,
474 Fig. 4a-d). We then take the resulting patterns of freshwater fluxes and scale them up and down,
475 varying from 0.1 to 2 times the "present-day" case (vertical axes, Fig. 4a-d). Note that if we assume
476 that freshwater transport to the subpolar regions scales as atmospheric water vapor content, we
477 would expect a doubling or halving of the flux to be associated with a 10°C change in temperature.
478 Each model is run for 2000 years. We then repeat this set of experiments using a counterfactual
479 case where the freshwater flux is higher in the Pacific than in the Atlantic ($F_w^{npac} = 0.6$ Sv).

480 Both the Atlantic (Fig. 4a and c) and Pacific overturning (Fig. 4 b and d) show a strong sensitivity
481 to the relative size of the interbasin transport (horizontal axis) and amplitude (vertical axis) of the
482 hydrological cycle. Starting with a baseline present-day configuration in which $F_w^{IB} = 0.15$ Sv with
483 hydrological amplitude set equal to 1, we find that we can turn off the overturning in the Atlantic
484 (Fig. 4a) either by increasing the amplitude of the hydrological flux, or by changing the direction

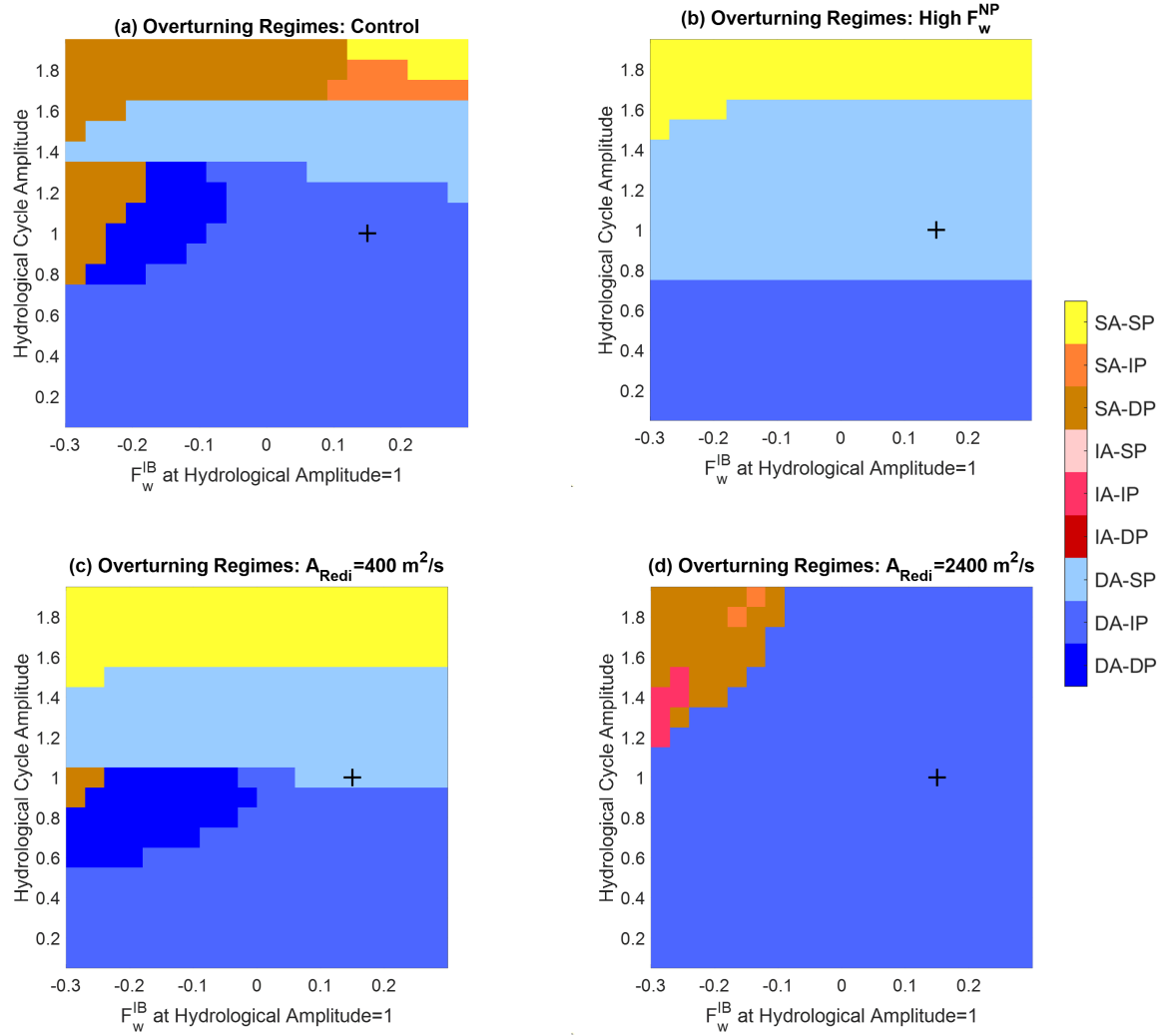


485 FIG. 4. Dependence of overturning circulation (Sv) in Atlantic (a and c) and Pacific (b and d) as a function
 486 of configuration and amplitude of the hydrological cycle for simulations started with observed initial conditions
 487 and run for 2000 years. In each subplot the horizontal axis shows a particular change in the configuration of
 488 the hydrological cycle (F_w^{IB} relative to all the other fluxes). The scale shows the value of F_w^{IB} in Sv when the
 489 hydrological cycle amplitude is 1. The amplitude of the hydrological cycle is shown along the vertical axis. Plus
 490 marks show our estimate of the present-day fluxes. The top row (a and b) shows an experiment where, at the
 491 hydrological amplitude of 1, the North Pacific freshwater flux F_w^{npac} is the observationally constrained value of
 492 0.34 Sv (smaller than North Atlantic- so that the poleward freshwater transport acts to make the North Atlantic
 493 less salty with respect to the North Pacific). The bottom row (c and d) shows an experiment where $F_w^{npac}=0.6$ Sv
 494 at hydrological cycle amplitude of 1, so that the poleward freshwater transport makes the North Atlantic saltier
 495 with respect to the North Pacific.

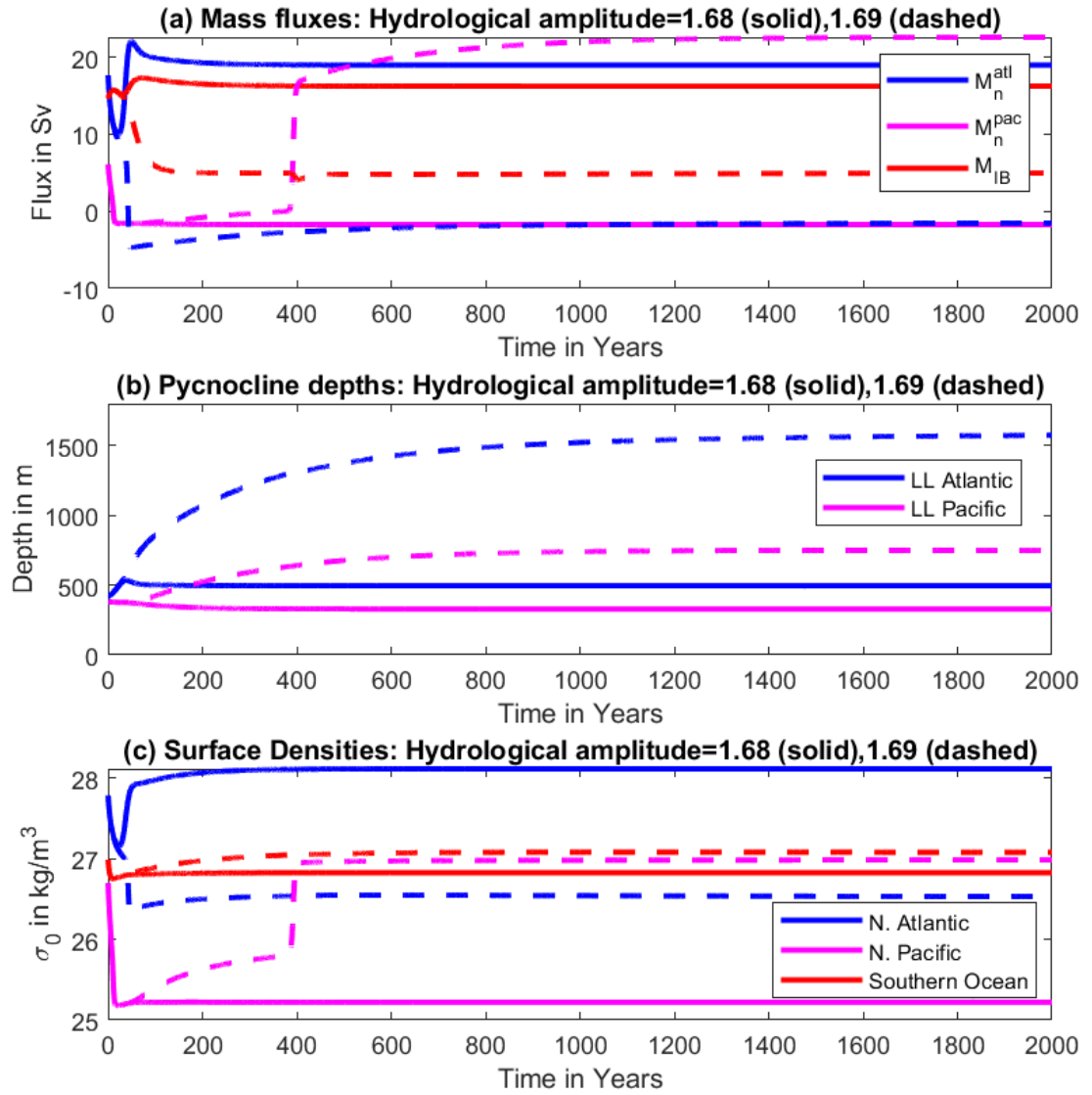
496 of the interbasin atmospheric freshwater transport. The behavior of the Pacific overturning (Fig.
497 4b) is even more interesting. Starting from our baseline case, we can increase the overturning by
498 decreasing the amplitude of the hydrological cycle (which reduces the contrast in salinity between
499 the Pacific and the Atlantic), reversing the interbasin atmospheric transport so that it goes from the
500 Pacific to the Atlantic (ditto) or *increasing* the amplitude of the hydrological cycle. *We are thus*
501 *able reproduce the qualitative behavior whereby the overturning in the Pacific can strengthen in*
502 *either warmer or colder climates.*

503 We can formalize these differences in overturning regimes by constructing a phase diagram of
504 the overturning as a function of hydrological configuration and amplitude. As shown in Fig. 5
505 we color-code the different states, going from cooler to hotter colors as the overturning shallows
506 in the Atlantic and darker to lighter colors as it shallows in the Pacific. In the control case the
507 dominant regime at lower values of hydrological cycling is DA-IP, consistent with the fact that
508 our target North Pacific Intermediate Water is lighter than both Antarctic Intermediate Water and
509 North Atlantic Deep Water. A strong enough hydrological cycle with initial conditions similar to
510 today can access either the SA-IP or the SA-SP states (orange colors in upper right of the plot).
511 However, if we reverse the interbasin flux, we can enter a regime where both basins show deep
512 water formation (dark blue region in Fig. 5a where the hydrological cycle amplitude is near 1 and
513 there is a moderate flux from the Pacific to the Atlantic). A strong enough reverse flux can produce
514 a SA-DP state (brown).

515 The counterfactual case shows a much simpler response: overturning shuts down as the amplitude
516 of the hydrological cycle increases (move from bottom to top)- first in the Pacific (Fig. 4d), then in
517 the Atlantic (Fig. 4c). Changing the interbasin atmospheric water transport F_w^{IB} has relatively little
518 impact on the parameter dependence of overturning over the range shown. However, reversing it
519 so that it dumps freshwater into the Atlantic does result in a Pacific overturning that is slightly
520 more stable to increases in hydrological cycle amplitude, as well as an Atlantic overturning that is
521 slightly less stable. The phase diagram for this case (Fig. 5b) shows only three of the six states
522 seen in the Control simulation for the range of parameters covered here- DA-IP at low levels of
523 hydrological cycling, DA-SP at levels comparable to the present day and SA-SP at high levels of
524 cycling.



525 Fig. 5. Classifying global overturning configurations depending on whether Deep, Intermediate or Surface
 526 waters are primarily formed in the Atlantic and Pacific. As we move from cooler (blue) to warmer (brown/yellow)
 527 colors, Atlantic circulation shallows. As we move from darker shades to lighter ones, Pacific circulation
 528 shallows. Axes as in Fig. 4. Plus marks show "present-day" hydrological state. (a) Control simulation
 529 ($A_{Redi} = 1000 \text{ m}^2 \text{s}^{-1}$, $F_w^{npac} = 0.34 \text{ Sv}$). (b) Higher Pacific freshwater flux. $F_w^{npac} = 0.6 \text{ Sv}$. (c) Lower lateral
 530 mixing ($A_{Redi} = 400 \text{ m}^2 \text{s}^{-1}$). (d) Higher lateral mixing ($A_{Redi} = 2400 \text{ m}^2 \text{s}^{-1}$).



532 FIG. 6. Evolution of the (a) Large-scale circulation; (b) Pycnocline depths in Atlantic and Pacific; and (c)
 533 densities in two cases near a tipping point. Solid lines show case where a hydrological cycle with the baseline
 534 geometry has its amplitude instantaneously increased by a factor of 1.68. Dashed lines show a case where it is
 535 increased by a factor of 1.69.

531 *b. Understanding how the overturning "tips" to the Pacific at high freshwater flux*

536 The eventual tipping of the dominant overturning location to the Pacific within our model is
537 sensitive to very small changes in freshwater flux. As shown in Fig. 6a, instantaneously increasing
538 the hydrological cycle from our base case by a factor of 1.68 (solid lines) results in a collapse of
539 the North Pacific overturning (solid magenta line). There is an initial drop, but then a recovery of
540 the North Atlantic overturning (solid blue line), resulting in a final DA-SP regime. Increasing the
541 scaling factor to 1.69 (dashed lines) produces an almost identical initial drop in both overturning
542 circulations, but with the North Atlantic then proceeding all the way to collapse as well, giving
543 us a temporary SA-SP configuration between years 50 and 400. After this we see another rapid in
544 increase in the overturning in the North Pacific, which stabilizes at of 20 Sv. Note however, that
545 the North Pacific subpolar box stays lighter than the Southern Ocean surface box (magenta dashed
546 line stays below the red dashed line in Fig. 6c), so that the new state corresponds to a SA-IP ocean
547 rather than a SA-DP ocean.

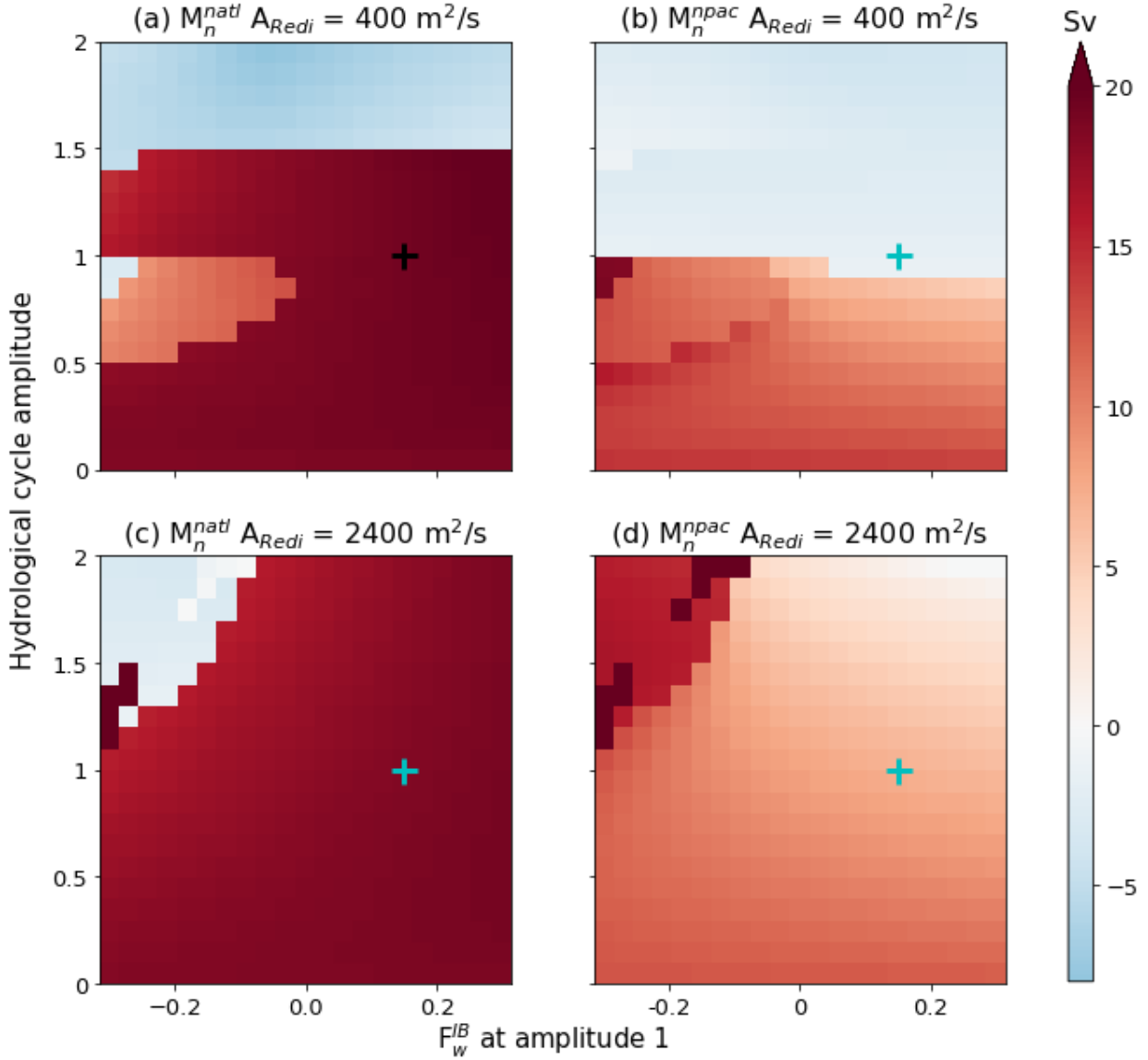
548 What accounts for the re-establishment of overturning in the Pacific in the case with a step
549 change to 1.69 the hydrological amplitude? Note that within this case the establishment of an
550 SA-SP circulation involves an initial reverse circulation of about -4.5 Sv in the Atlantic and -1.5
551 Sv in the Pacific, as the freshening of the North Pacific and Atlantic makes them lighter than
552 the tropics in both basins. However, over time, the density in both subpolar basins rises and the
553 magnitude of the overturning decreases (reflecting a smaller rise in pressure between the tropics
554 and the subpolar gyre), pointing to a decrease in the density gradient between fresh, light subpolar
555 water and saltier, heavier tropical water. This decrease in gradient is driven by both northern
556 subpolar basins becoming saltier (not shown here) relative to their corresponding tropical basins.
557 Because this increase in the salinity is occurring in the face of a weakening supply of salty water
558 from the overturning, it must be driven by the only remaining term in the salt budget, namely the
559 mixing flux. As can be seen in Fig. 6b, once the overturning circulation shuts off, the pycnocline
560 in both the Atlantic and Pacific deepens. Over time this causes the mixing flux (which we have
561 parameterized in equation 14 to scale as low-latitude pycnocline depth) to increase to about 6 Sv
562 in both basins, even as the overturning drops. In the Pacific this increase in mixing allows the
563 subpolar basin to become dense enough to start sinking, at which point the freshwater gets flushed
564 out of the system.

565 c. Sensitivity to subgridscale eddy mixing

566 While there are a host of parameters that can affect the overturning circulation, we focus particu-
567 larly on one, the lateral diffusion coefficient A_{Redi} that governs the horizontal diffusive exchange of
568 heat and salt between the low-latitudes and the high latitudes. Within a recent generation of climate
569 models A_{Redi} was found to vary from less than $400 \text{ m}^2 \text{ s}^{-1}$ to $2000 \text{ m}^2 \text{ s}^{-1}$ (Abernathay et al. 2022).
570 As already noted, previous research from the Gnanadesikan group (Pradal and Gnanadesikan 2014;
571 Bahl et al. 2019) has shown that this uncertainty is important, as changes over this range within a
572 single model can affect the overturning in both the Atlantic and Pacific oceans.

573 Reproducing the sensitivity study of Fig. 4a and b with the control values for F_w^{npac} but with
574 either lower ($400 \text{ m}^2 \text{ s}^{-1}$, top row of Fig. 7) or higher ($2400 \text{ m}^2 \text{ s}^{-1}$, bottom row of Fig. 7) values for
575 A_{Redi} reveals a strong sensitivity to this parameter in the box model. For lower values of A_{Redi} ,
576 given modern values of freshwater fluxes, the overturning in the Pacific reverses. The Atlantic
577 overturning with observed fluxes is slightly stronger than with the control $A_{Redi} = 1000 \text{ m}^2 \text{ s}^{-1}$
578 (with a value of 19.3 Sv). However, if we change the interbasin freshwater transport (moving to
579 the left from the cross mark) the North Atlantic is more resistant to collapse. It is only a little
580 less stable to increases in the hydrological cycle, with a collapse occurring near an amplitude of
581 1.58 rather than 1.68. This can also be seen by comparing the brown areas in Fig. 5a and c.
582 A notable contrast with our control simulation is that turning off the North Atlantic overturning
583 does not result in overturning switching to the Pacific for positive values of interbasin flux (Fig.
584 5c), because the lower mixing coefficient means that the lateral mixing is not sufficiently strong
585 to degrade the freshwater cap in the Pacific. Only if the interbasin flux reverses do we see the
586 overturning shift to the Pacific.

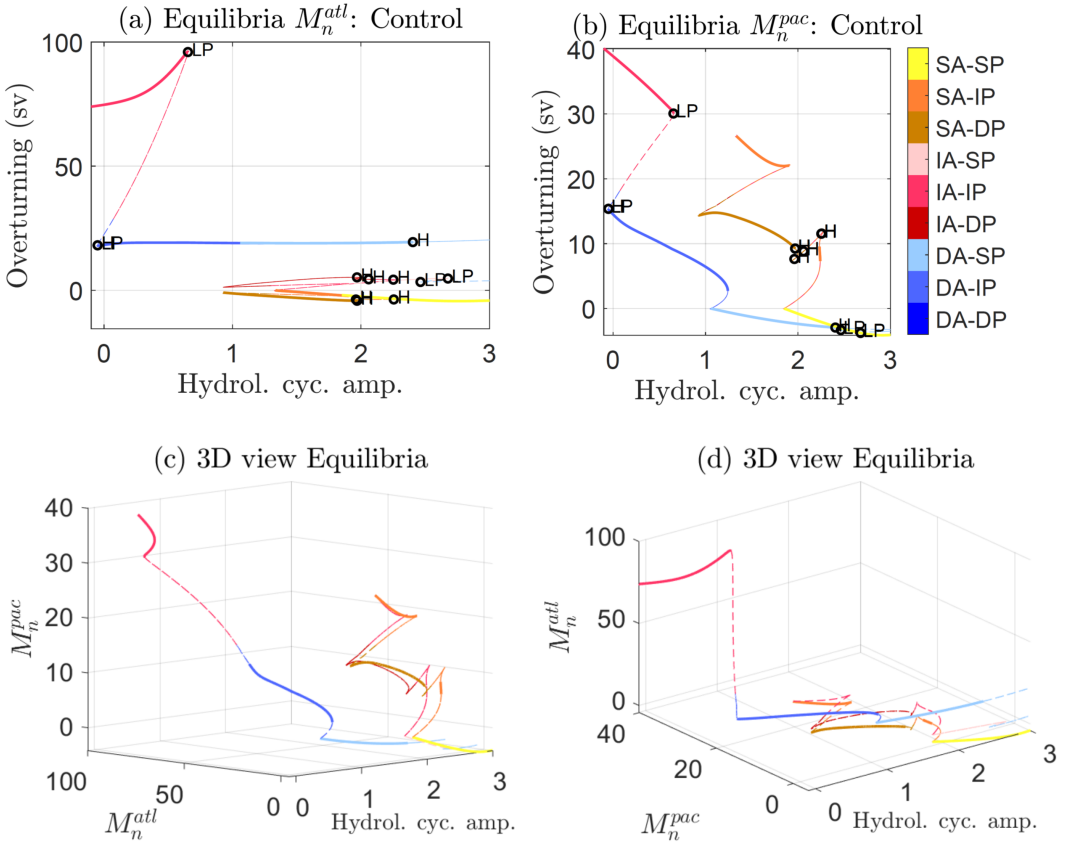
587 Increasing the mixing coefficient to $2400 \text{ m}^2 \text{ s}^{-1}$ (bottom row of Fig. 7), on the other hand,
588 produces a somewhat larger (8 Sv vs 6 Sv in the control) Pacific overturning in the base case.
589 The overturning configuration in this case is significantly more stable to changes in both interbasin
590 flux and amplitude of the hydrological cycle. Interestingly, reversing the interbasin freshwater flux
591 with higher mixing can produce an IA-IP state (dark pink, Fig. 5d), which does not appear in the
592 other scenarios.



573 FIG. 7. Same as Fig. 4 except at varying values of subgridscale lateral eddy mixing parameter A_{Ready} . The
 574 top row (a and b) shows the Atlantic and Pacific overturning (Sv) respectively, with $A_{Ready} = 400 \text{ m}^2/\text{s}$, near the
 575 lower end of the current value used in climate models. The bottom row (c and d) show the Atlantic and Pacific
 576 overturning (Sv) respectively, with $A_{Ready} = 2400 \text{ m}^2/\text{s}$ near the top end of the current value used in climate
 577 models.

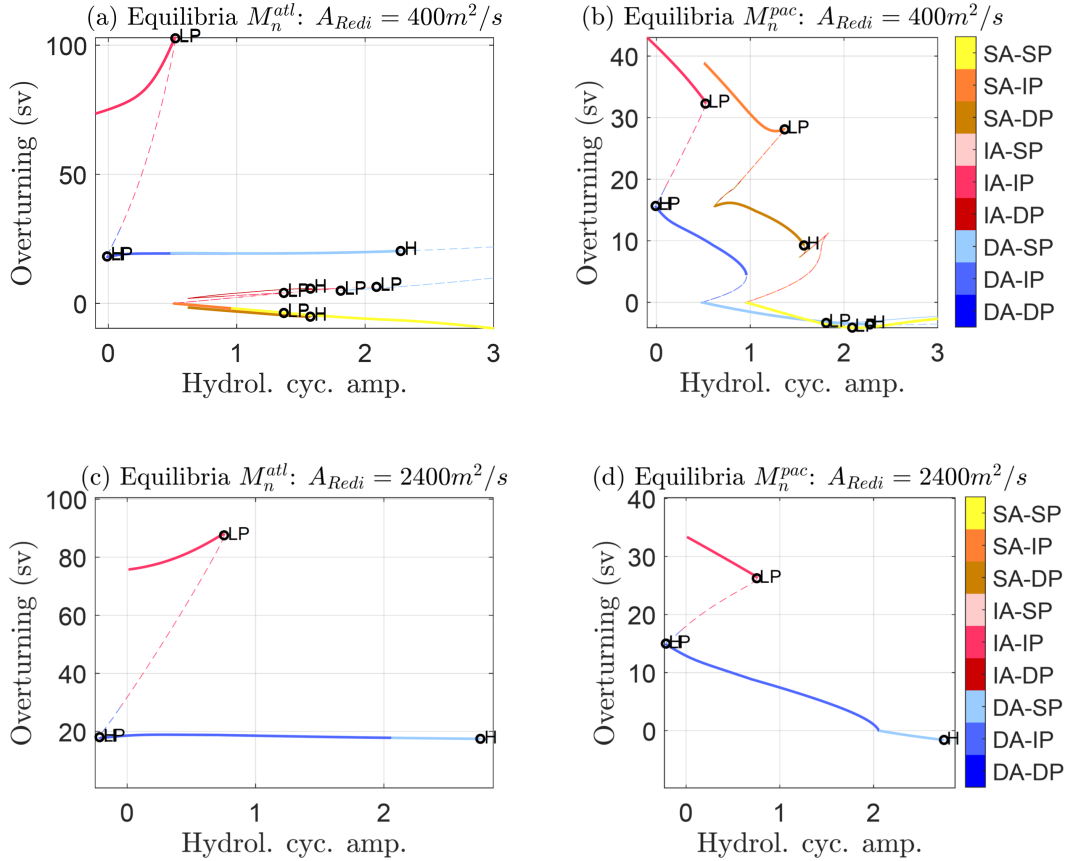
598 *d. Bifurcation analysis-Baseline case*

608 The results presented up to this point assume a particular set of initial conditions (corresponding to
 609 the present-day) and an instantaneous change of the amplitude or configuration of the hydrological



599 FIG. 8. Numerical bifurcation diagrams with respect to the amplitude of the hydrological cycle showing steady
600 states of the overturning for the baseline parameter set. All states computed using the matCont code. Colors as
601 in Fig. 5. Limit points are marked with "LP", Hopf bifurcations with "H". Thick solid lines show stable steady
602 states, thinner dashed lines show unstable steady states. (a) North Atlantic overturning M_n^{atl} (b) North Pacific
603 Overturning M_n^{pac} (c,d). Two three-dimensional views of the solution space plotting M_n^{atl} and M_n^{pac} against
604 hydrological cycle amplitude.

610 cycle. However, it turns out that if we use numerical continuation methods to allow for quasi-
611 static changes in parameters and to explore a wider range of initial conditions, we can find multiple
612 equilibrium states while only changing the amplitude of the hydrological cycle. This is summarized



605 FIG. 9. Same as Fig. 8 a and b but now varying the lateral mixing coefficient A_{Redi} . (a) Atlantic overturning
 606 for low lateral mixing ($A_{Redi} = 400 \text{ m}^2 \text{s}^{-1}$). (b) Same as (a) but for Pacific. (c) Atlantic overturning for high
 607 lateral mixing. ($A_{Redi} = 2400 \text{ m}^2 \text{s}^{-1}$). (d) Same as (c) but for Pacific. Colors as in Figs. 5, 8.

613 for the baseline parameter set in Fig 8, which looks at steady states as functions of the amplitude of
 614 the hydrological cycle. In this and the following figure, geometric configurations of the overturning
 615 are denoted in the same colors as in Fig. 5 with stable branches denoted with thick solid lines and
 616 unstable branches denoted with thin dashed ones. The results show a number of surprises.

617 First, consider what happens if we start from our baseline case (which we would describe as
 618 DA-IP) at a value of 1 for the hydrological cycle amplitude and around 19 Sv for M_n^{atl} . As we

increase the freshwater forcing (moving to the right along the blue curve in Fig. 8a) the overturning in the Atlantic is remarkably steady, while the Pacific overturning collapses. The collapse of the North Pacific overturning (blue lines in Fig. 8b) as we increase the freshwater flux looks very much like the classic Stommel fold bifurcation, with a transition to a DA-SP state. Analysis of the eigenvalues of the Jacobian at this point shows that this is, in fact, a limit point bifurcation. Though it is not visible on this plot, the collapse of the North Pacific overturning actually results in a slight *increase* in the North Atlantic overturning. As the freshwater flux continues to increase, there is eventually a Hopf bifurcation (indicated by the H on the light blue line in Fig. 8a) at a hydrological cycle amplitude of around 2.3 times the control value. At this point there is a transition to an SA-SP state (with the solid yellow lines being the only stable states at large hydrological cycle amplitudes), with deep pycnoclines in both basins and very fresh northern surface boxes.

The other configurations found in Fig. 5 when initializing our model from modern conditions also show up when tracing out stable and unstable manifolds using continuation methods. If we look the lower left of the Figs. 8a and b, we see a complicated network of curves. When plotted in 3 dimensions (Fig. 8c,d), we see that these curves correspond to several manifolds with weak surface or intermediate overturning in the Atlantic and intermediate or deep overturning in the Pacific. The solution illustrated in Fig. 6 is one of a manifold of states given by the thick orange curve between hydrological amplitudes of 1 and 2, M_n^{pac} in the 22-28 Sv range and M_n^{atl} between 0 and -5 Sv. This manifold is "connected" to other states via an unstable IA-IP manifold (thin red curves). Additionally, there is a manifold corresponding to a SA-DP state (brown curve) with M_n^{pac} in the 10-15 Sv range and a M_n^{atl} between -5 and 0 Sv. In Fig. 5a, SA-DP states are only found by changing both the amplitude of the hydrological cycle and the relative size of the interbasin transport- here we are able to get them by changing initial conditions. Note that while the stable SA-DP manifold is connected to the SA-IP manifold by an unstable manifold (thin brown-orange line best seen in Fig. 8b,c) it is not obvious that a model reaching the end of one of these stable manifolds will transition between them.

There is also a branch with very high overturning in both the Atlantic and Pacific at low freshwater flux (red curves). This branch turns out to represent an IA-IP case in which there is a very strong flow of warm tropical water to high latitudes in both basins, such that the atmosphere is not able to cool the water enough to make it denser than the Southern Ocean. For our baseline parameter set,

649 this branch is only stable at hydrological cycle amplitudes lower than the present day. Note that
650 these states do not appear in Fig. 5a, so that they cannot be easily accessed from modern initial
651 conditions via instantaneous changes in the hydrological cycle- again highlighting the utility of
652 continuation methods in exploring the possible range of solutions.

653 The dependence of these regimes on hydrological cycle amplitude is sensitive to the paramet-
654 erization of mixing. For $A_{Redi} = 400 \text{ m}^2 \text{s}^{-1}$ (Fig. 9 a,b) the dependence is similar to that at
655 $A_{Redi}=1000 \text{ m}^2 \text{ s}^{-1}$ but all states shift to the left, with SA-SP (orange curves) states permitted at
656 much lower hydrological cycle amplitudes and associated with larger values of M_n^{pac} (note differ-
657 ence between the range of the thick orange curves in Fig. 9b and 8b). Interestingly, while the IA-IP
658 (red curves in upper left of plot) configuration collapses at a lower amplitude of hydrological cycle
659 than is seen in Fig. 8a,b, lower A_{Redi} allows for higher overturning transports.

660 For the higher mixing case ($A_{Redi} = 2400 \text{ m}^2 \text{s}^{-1}$, Fig. 9c,d) we see the reverse effect: the IA-IP
661 state is weaker at any given hydrological cycle amplitude, but persists to greater hydrological cycle
662 amplitude. At high hydrological amplitudes we no longer see the SA states (no orange, yellow
663 or brown curves near the bottom of Fig. 9c). Instead, when we run the model in this parameter
664 range what appears is a limit cycle in which there are multicentennial bursts of DA-SP states which
665 drain the pycnocline interspersed with multicentennial SA-IP states where the pycnocline slowly
666 deepens. Detailed investigation of these states is deferred to a future manuscript.

667 *e. Response to global temperature changes*

668 Up to this point we have focused on changes in the geometry and amplitude of the hydrological
669 cycle alone, without considering a primary driver of such changes, namely global temperatures.
670 While a full discussion of the sensitivity to global warming is beyond the scope of this manuscript,
671 we present some preliminary exploration of changing temperatures and hydrological cycle together.
672 We consider two cases. In the first, we impose a globally uniform change in the atmospheric
673 restoring temperatures with an associated increase of the hydrological cycle amplitude of 7% per
674 degree. This scaling is what we would expect if transport scaled as water vapor content. In the
675 second set of simulations, we allow for polar amplification in the northern hemisphere high latitudes
676 but reduced warming in the Southern Hemisphere high latitudes. For this set of simulations we
677 use a factor of 1.5 for the high latitude Northern Hemisphere and 0.6 for the high-latitude Southern

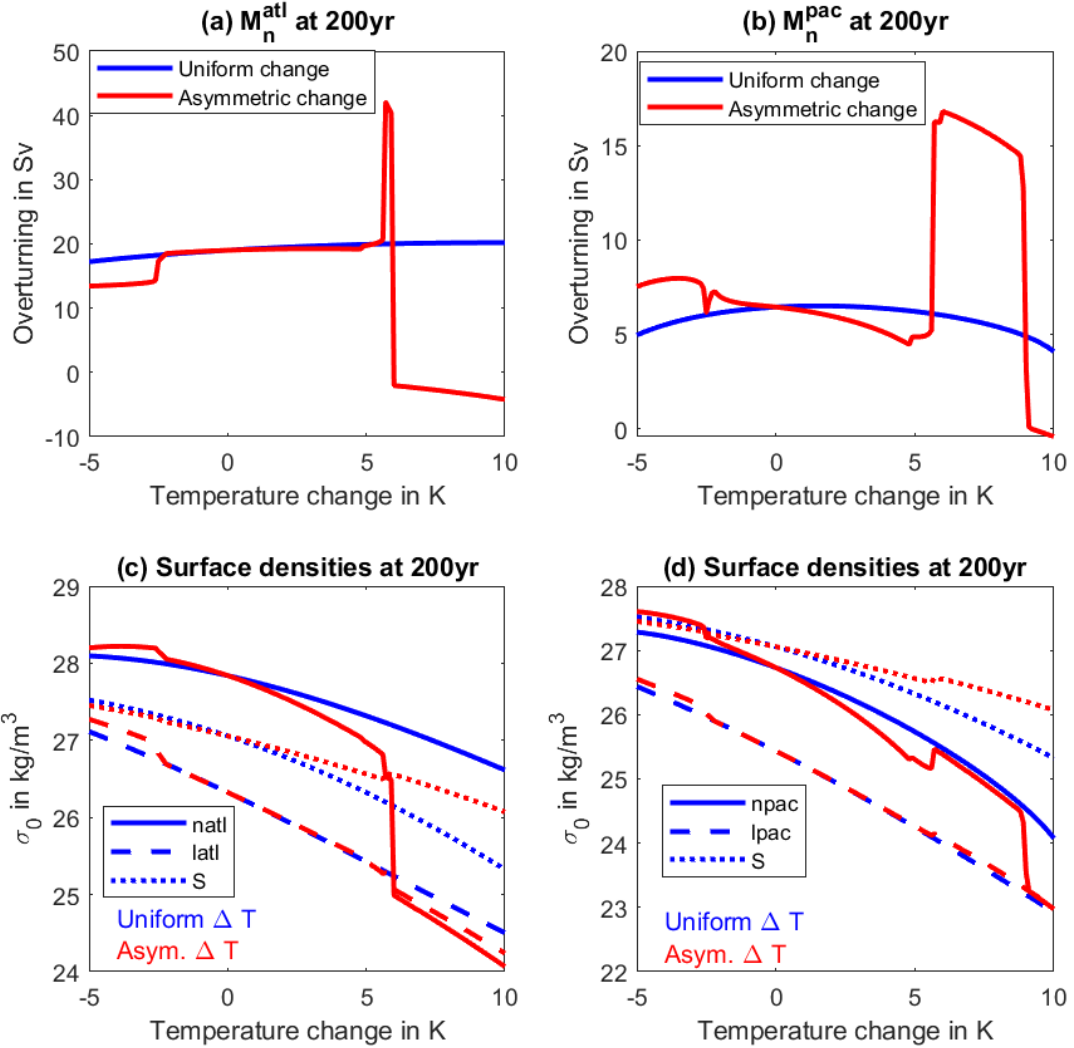
678 Hemisphere. These values are typical of the net warming of the atmosphere over the polar oceans
679 in the GFDL ESM2Mc models, and are consistent with the CMIP6 suite of models (Hahn et al.
680 2021). In all cases we started our simulations from the same initial conditions and parameter sets
681 as in the control simulation and integrated for 200 years in order to make our simulations more
682 comparable with those carried out for the IPCC process.

683 As shown by the blue lines in Fig. 10a,b the overturning in both basins is surprisingly insensitive
684 to a uniform change in temperature. This is understandable if we consider the response of the surface
685 densities to climate change (Fig. 10c,d). Under uniform temperature change (blue lines), all
686 densities show a similar value of change. As temperature increases, the decrease in density gradient
687 between the northern and low latitudes due to increased freshwater flux is largely compensated by
688 the increase in the sensitivity of density to temperature. The idea that higher temperatures might
689 compensate higher freshwater fluxes due to non-linearities of the equation of state was previously
690 advanced by De Boer et al. (2007) and Schloesser (2020).

691 Under an asymmetric temperature change, however, the overturning shows more complex be-
692 havior (red lines, Fig. 10). At low temperatures, the North Pacific becomes denser than the Southern
693 Ocean due to a combination of a.) the Southern Ocean restoring temperature dropping less than the
694 North Pacific and b.) the fact that in our model the restoring temperature is lower in the North Pacific
695 than in the Southern Ocean to begin with. As a result, deep water can form there. The opening of a second
696 deep water pathway "steals" some of the overturning from the Atlantic for cooling below about 2°C (note
697 the dip in the red line at low temperatures in Fig 10a). As temperatures warm, on the other hand, the
698 North Atlantic sees its density drop faster than the Southern Ocean. At a warming of around 4.7°C this
699 results in a transition to an IA-IP circulation, with an associated deepening of the pycnocline (not shown)
700 and for warming just short of 6°C we see a collapse in both basins and an SA-SP regime. We note that we
701 expect these results to be strongly dependent on the degree of asymmetry in warming, the rate of warming
702 and internal parameters—all of which will be explored in future work.

710 4. Comparison with a fully coupled model

711 While a full calibration of our six-box model against an ESM is beyond the scope of this
712 paper (for reasons we will outline below), we can still use ESM simulations to support some of



691 FIG. 10. Overturning and surface densities given the baseline physical and model initial conditions 200 years
 692 after an abrupt change in temperature and associated change in the amplitude of the hydrological cycle. Uniform
 693 temperature change is shown in blue, hemispherically asymmetric (1.5 tropical value in north, 0.6 in south) in
 694 red. (a) North Atlantic overturning M_n^{atl} in Sv. (b) North Pacific overturning M_n^{pac} in Sv. (c) Densities in
 695 North Atlantic (solid), Low Latitude Atlantic (long dashed) and Southern Ocean (dotted). (d) Same as (c) but
 696 for Pacific.

713 the assumptions made to construct our box model and to demonstrate some similar changes in

714 overturning configuration. First, as CM2Mc is mass conserving in the ocean, we can use the
715 difference between mass transport across various lines to compute how much freshwater is added
716 to different regions. As shown in the top row of Table 3, the models all support the idea that net
717 freshwater fluxes into the Arctic and subpolar North Atlantic are larger than net freshwater fluxes
718 into the subpolar North Pacific.

722 Matching watermass properties is challenging in high latitudes, in part because the regions where
723 deep water forms are often different in the model vs. in observations. For purposes of this paper,
724 we take densities in the Atlantic from 55-65°N and 60-20°W at depths from 100-400m which is
725 where the near-surface waters with densities corresponding to the model NADW are found in the
726 main Atlantic. In the North Pacific, we look at waters between 100-400m between 55 and 65°N. In
727 the Southern Ocean we look for waters between the surface and 400m between 55 and 50°S. The
728 resulting watermass properties in the low mixing (AREDI400) control simulation are qualitatively
729 similar to the our box model results, with the North Atlantic being the densest of the polar boxes,
730 followed by the Southern Ocean and then the North Pacific. The density difference between the
731 tropics and North Atlantic is 1.64 kg m^{-3} while that in the Pacific is about 1.49 kg m^{-3} , slightly
732 larger than the 1.42 and 1.23 kg m^{-3} seen in our target values. With relatively realistic pycnocline
733 depths (409 in the Atlantic and 388 in the Pacific) we can invert for the resistance parameter ϵ by
734 plugging in the overturning in the two basins near its maximum latitude. This yields a resistance
735 parameter of $1.21 \times 10^{-4} \text{ s}^{-1}$ in the Atlantic (again in line with our previous estimates) and $2.71 \times$
736 10^{-4} s^{-1} in the Pacific, qualitatively similar to the factor of 2 increase in equation (17).

737 When the A_{Redi} coefficient is increased, we see a salinification of the North Pacific (1.13 PSU)
738 and Southern Ocean (0.44 PSU). The result is to increase the density in the North Pacific so that
739 it is greater than in the Southern Ocean. The resulting overturning is actually larger in the Pacific
740 than in the Atlantic, and the resulting ϵ is $0.94 \times 10^{-4} \text{ s}^{-1}$. Meanwhile, M_n^{atl} drops slightly, from
741 21.7 to 18.0 Sv.

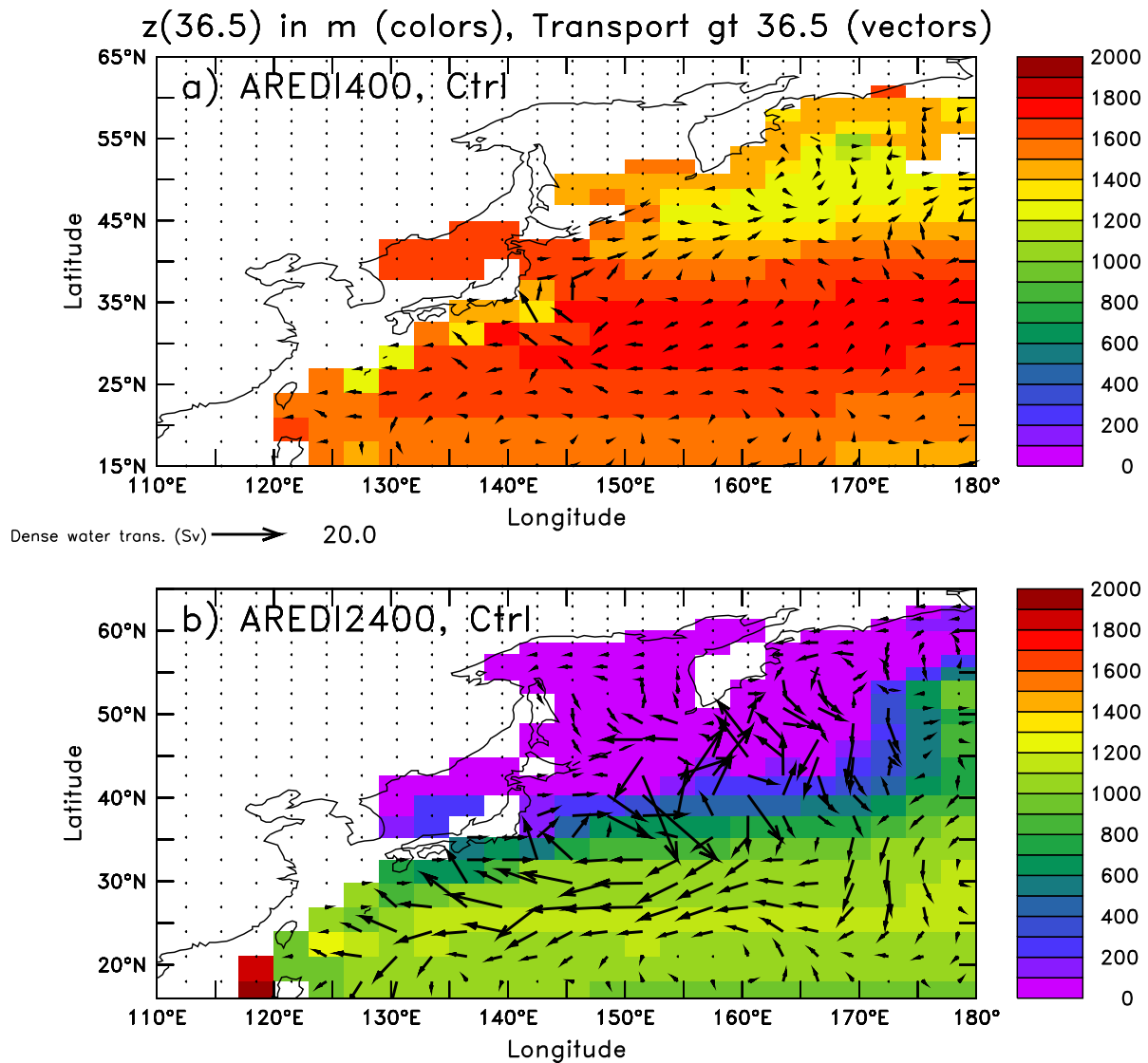
742 In our baseline box model a change in A_{Redi} from 400 to 2400 $\text{m}^2 \text{s}^{-1}$ results in North Pacific
743 salinity increasing sharply from 31.5 PSU to 34.2 PSU, and the overturning switching from an
744 DA-SP configuration with $M_n^{pac} = -1.6 \text{ Sv}$ to a DA-IP configuration with $M_n^{pac} = 7.9 \text{ Sv}$. However
745 in the baseline box model the change in Southern Ocean salinity from 33.99 to 34.24 is smaller
746 than in the coupled model and does not result in the Southern Ocean becoming denser than the

719 TABLE 3. Simulation results from four Earth System Models run with different values of lateral mixing
 720 coefficient A_{Redi} (400 and 2400 m^2s^{-1}) and two levels of CO₂ (control simulation is 286 ppmv, 2xCO₂ is 572
 721 ppmv). All results represent average over final century of simulation.

Output/Simulation	AREDI400 CTRL	AREDI2400 CTRL	AREDI400 2xCO2	AREDI2400 2xCO2
$F_w^{natl}, F_w^{npac}, F_w^{SO}$	0.34,0.28,0.65	0.39,0.23,0.65	0.41,0.31,0.76	0.45,0.28,0.77
$T_{natl}, S_{natl}, \rho_{natl}$	5.73, 35.10, 27.65	5.54, 35.20, 27.76	4.53, 34.65, 27.43	5.88, 35.13, 27.66
$T_{latl}, S_{latl}, \rho_{latl}$	16.08, 35.50, 26.01	16.05, 35.74, 26.19	17.35, 35.80, 25.95	17.53, 36.03, 26.07
$T_{npac}, S_{npac}, \rho_{npac}$	2.04, 33.24, 26.50	3.79, 34.35, 27.25	3.44, 33.02, 26.22	4.49, 34.03, 26.91
$T_{lpac}, S_{lpac}, \rho_{lpac}$	17.27, 34.63, 25.01	17.27, 34.98, 25.28	18.14, 34.52, 24.71	18.38, 34.89, 24.93
$T_{SO}, S_{SO}, \rho_{SO}$	5.34, 33.96, 26.79	5.59, 34.4, 27.09	5.78, 33.86, 26.65	6.58, 34.31, 26.90
$D_{low}^{natl,npac}$	409, 388	367,330	427,384	389,337
M_n^{atl}, M_n^{pac}	21.7, 8.0	18.0,21.6	16.6,7.1	16.7,13.3
ϵ_{natl}	1.21×10^{-4}	1.12×10^{-4}	1.55×10^{-4}	1.37×10^{-4}
ϵ_{npac}	2.71×10^{-4}	0.94×10^{-4}	3.01×10^{-4}	1.63×10^{-4}

747 North Pacific. Increasing A_{Redi} also causes M_n^{atl} to decline (from 19.3 to 18.5 Sv), smaller than
 748 the decline in the coupled models. However, as this change in mixing is insufficient to form deep
 749 water in the North Pacific we do not see a reduction in the pycnocline depth, which would drive
 750 larger reductions.

751 Under doubled CO₂, the freshwater fluxes in the coupled simulations increase sharply. In the
 752 AREDI400 simulation the global mean surface air temperature warms by 1.4°C while in the
 753 AREDI2400 simulation it warms by 1.7 °C. This implies a 14%/°C sensitivity of F_w^{natl} in the the
 754 AREDI400 case but a 9%/°C sensitivity in the AREDI2400 case. F_w^{npac} has a slightly different
 755 sensitivity, 7.7%/°C in the AREDI400 case but 10%/°C sensitivity in the AREDI2400 case. This
 756 suggests that while the rough 7%/°C Clasius-Clapeyron-based scaling used in the box model is not
 757 wildly inaccurate, it likely underestimates some of the impacts due to changes in circulation. As
 758 expected, the increase in freshwater flux leads to increased salinity in the tropics and decreased
 759 salinity in the high latitudes. Note however, that this does not necessarily result in a decreased
 760 density contrast within a given basin. This highlights the utility of using a nonlinear equation of
 761 state in our box model, which leads to a greater focus on the role of changes in pycnocline depth
 762 and ϵ under climate change. It also supports the conclusion of De Boer et al. (2010) that a simple
 763 linear scaling between density contrast and overturning is insufficient to explain key aspects of
 764 overturning.



765 FIG. 11. Change in density structure and overturning associated with changing lateral mixing coefficient A_{REDI}
 766 in CM2Mc model of Galbraith et al. (2011). Colors show depth in m of the $\sigma_2 = 36.5$ isopycnal surface. σ_2 is
 767 used here because CM2Mc saves transports in density space in this coordinate system. Vectors show transport of
 768 water denser than this surface. (a) AREDI400 simulation showing that this surface is deep and circulation below
 769 it is relatively weak. (b) AREDI2400 simulation showing that the surface outcrops in the Northwest Pacific and
 770 that there is flow away from the outcrop in the eastern sector of the plot, but flow back towards the outcrop in
 771 western sector.

772 In the AREDI400 case, the overturning decreases by about 5 Sv (23%) in the North Atlantic and
773 0.9 Sv ($\sim 11\%$) in the North Pacific. In the AREDI2400 case, however, both the absolute and
774 relative decline in the North Pacific (8.3 Sv, 38%) are much larger than the absolute and relative
775 decline in the North Atlantic (1.3 Sv, 7%). Note that in the AREDI2400 case, the density of the
776 Southern Ocean approaches that of the North Pacific, but remains much heavier than the North
777 Atlantic and that this is associated with a sharp increase in ϵ . Again this qualitatively supports
778 our approach of considering all three polar basins when thinking about changes in overturning
779 configuration.

780 In summary, the coupled model simulations support a number of the choices made in configuring
781 our box model. 1. Having a larger freshwater flux to the Arctic+Subpolar Atlantic than the North
782 Pacific. 2. Including a nonlinear equation of state allowing for some compensation of changes in
783 salinity and temperature. 3. Allowing for relatively larger responses in atmospheric freshwater
784 transport to temperature change than is generally associated with global precipitation (which is
785 dominated by the tropics). 4. Allowing for the resistance to overturning to depend on the contrast
786 between the northern and Southern subpolar basins. While the dependence of ϵ on density structure
787 is clearly more complicated than that in equation 17, we clearly see that having the density of the
788 Southern Ocean approach that of the northern subpolar oceans is associated with a less efficient
789 conversion of APE into overturning.

790 5. Discussion

791 We have developed a framework for understanding the competing roles of the geometric configu-
792 ration of the atmospheric hydrological cycle, the amplitude of the atmospheric hydrological cycle,
793 and oceanic eddy processes in setting the configuration and magnitude of the ocean circulation.
794 Key lessons that emerge are: 1. Given a freshwater flux to the Arctic+Subpolar North Atlantic that
795 is larger than the freshwater flux to the subpolar North Pacific, the North Pacific overturning can
796 increase as a result of either increases or decreases in hydrological cycle amplitude. This is likely
797 to be a very different result than would be found from using idealized models with strip continents-
798 highlighting a potential deficiency in the configuration of such models. 2. We can qualitatively
799 explain the sensitivity of the overturning circulation to the lateral eddy mixing A_{Redi} , a parameter
800 that has been previously shown to have an important impact on overturning configuration in fully

801 coupled models. 3. Including two basins and interhemispheric control of overturning efficiency
802 allows for a number of interesting transitions across a range of overturning configurations.

803 We have only begun to scratch the surface of the parametric dependence of this model. We note
804 that, even for our simple model, we have over twenty initial conditions, physical parameters, and
805 boundary conditions-making a comprehensive exploration of the search space challenging. We are
806 currently exploring two approaches to this. One is to use the continuation methods outlined above
807 to search for interesting phenomena. The second is using generalized adversarial networks to trace
808 out the separatrices in state space between different dynamical states. Early results of the second
809 approach are reported in Sleeman et al. (2023a,b).

810 In constructing our model we have tried to strike a balance between a parsimonious representation
811 of the processes involved and a sufficiently comprehensive inclusion of key processes. That said,
812 it should be recognized that there are a number of processes that could benefit from a more
813 sophisticated treatment. One obvious shortcoming of our formulation is how we handle the
814 transition as the Southern Ocean becomes lighter/denser than the high latitude boxes. Explicitly
815 resolving an intermediate water box as in Alkhayou et al. (2019) would allow for a better treatment
816 of this, but would add additional parameters that are harder to constrain. This could be attacked by
817 analyzing experiments with full general circulation models in which the densities of NPIW, AAIW,
818 and tropical waters in the Pacific as well as Southern Ocean winds are changed separately, similar
819 to the work of Fučkar and Vallis (2007), but with realistic geometry and fixed freshwater fluxes.

820 It is also worth noting that the full three-dimensionality of the system can complicate fitting box
821 models to GCMs. When we examine transports in potential density space (computed in CM2Mc
822 using σ_2) increasing A_{Redi} results in changes both to the density structure and the overturning. In
823 the AREDI400 case, $\sigma_2 = 36.5$ never outcrops in the northwest Pacific (Fig. 11a), while in the
824 AREDI2400 case (Fig. 11b) it does. Looking at the transport of water denser than this surface
825 in AREDI2400 case reveals a recirculating flow. Dense waters are formed at relatively shallow
826 depths and injected into the interior at a number of locations east of 150°E and flow southward
827 below a sinking density surface. A significant fraction of this water, however, returns to the surface
828 waters west of 150°E. When we look at the zonally-integrated average in either depth or density, we
829 see significant cancellation of this flow, with only about 13 Sv of dense water moving southward
830 at 15°N. While one can think of this circulation as being encompassed by the exchange terms

831 $M_{LN,LS}$, we cannot simply parameterize it as we have done in equation 14 using a global diffusion
832 coefficient. Similar issues of how to divide recirculating flow from net transport arise in tracing
833 the interbasin flow- one reason why we do not explore it in more detail here.

834 Additionally, at this point we have treated the deep ocean as a single box and do not resolve
835 the different impacts of Antarctic Intermediate Water and Antarctic Bottom Water. Incorporating
836 more structure into the deep water (for example following ideas of Nikurashin and Vallis 2011)
837 would introduce additional time scales of variability and additional configurations of the circulation,
838 allowing us to better resolve the deep ocean circulation. However, it would also introduce additional
839 parameters, such as the magnitude and spatial distribution of the abyssal diapycnal and lateral
840 mixing coefficients.

841 Finally, in this paper we have ignored the presence of noise in the climate system. Including
842 noise in the model allows for a rich phenomenology of behavior including unsteady oscillations
843 and more complex transition behavior between states. We plan to report on these phenomena in
844 future publications.

845 *Acknowledgments.* This material is based upon work supported by the Defense Advanced Re-
846 search Projects Agency (DARPA) under Agreement No. HR00112290032. Approved for public
847 release; distribution is unlimited.

848 *Data availability statement.* Matlab codes to generate all the results used in this manuscript are
849 provided at 10.5281/zenodo.8126674.

850 **References**

851 Abernathey, R., A. Gnanadesikan, M.-A. Pradal, and M. A. Sundermeyer, 2022: Isopycnal mixing.
852 *Ocean Mixing*, Elsevier, 215–256.

853 Alkhayou, H., P. Ashwin, L. C. Jackson, C. Quinn, and R. A. Wood, 2019: Basin bifurcations,
854 oscillatory instability and rate-induced thresholds for atlantic meridional overturning circulation
855 in a global oceanic box model. *Proceedings of the Royal Society A*, **475** (2225), 20190 051.

856 Allgower, E. L., and K. Georg, 2012: *Numerical continuation methods: an introduction*, Vol. 13.
857 Springer Science & Business Media.

858 Allison, L., H. Johnson, D. Marshall, and D. Munday, 2010: Where do winds drive the antarctic
859 circum polar current? *Geophysical Research Letters*, **37** (12).

860 Bahl, A., A. Gnanadesikan, and M.-A. Pradal, 2019: Variations in ocean deoxygenation across
861 earth system models: isolating the role of parameterized lateral mixing. *Global Biogeochemical
862 Cycles*, **33** (6), 703–724.

863 Bryan, F., 1987: Parameter sensitivity of primitive equation ocean general circulation models.
864 *Journal of Physical Oceanography*, **17** (7), 970–985.

865 Burls, N. J., A. V. Fedorov, D. M. Sigman, S. L. Jaccard, R. Tiedemann, and G. H. Haug, 2017:
866 Active Pacific meridional overturning circulation (pmoc) during the warm Pliocene. *Science
867 Advances*, **3** (9), e1700156.

868 De Boer, A., D. M. Sigman, J. Toggweiler, and J. Russell, 2007: Effect of global ocean temperature
869 change on deep ocean ventilation. *Paleoceanography*, **22** (2), PA2010, <https://doi.org/doi:10.1029/2005PA001242>.

871 De Boer, A., J. Toggweiler, and D. M. Sigman, 2008: Atlantic dominance of the meridional
872 overturning circulation. *Journal of Physical Oceanography*, **38** (2), 435–450.

873 De Boer, A. M., A. Gnanadesikan, N. R. Edwards, and A. J. Watson, 2010: Meridional density
874 gradients do not control the Atlantic overturning circulation. *Journal of Physical Oceanography*,
875 **40** (2), 368–380.

876 DeVries, T., and F. Primeau, 2011: Dynamically and observationally constrained estimates of
877 water-mass distributions and ages in the global ocean. *Journal of Physical Oceanography*,
878 **41** (12), 2381–2401.

879 Dhooge, A., W. Govaerts, Y. A. Kuznetsov, H. G. E. Meijer, and B. Sautois, 2008: New features of
880 the software MatCont for bifurcation analysis of dynamical systems. *Mathematical and Computer
881 Modelling of Dynamical Systems*, **14** (2), 147–175.

882 Doedel, E., and L. S. Tuckerman, 2012: *Numerical methods for bifurcation problems and large-
883 scale dynamical systems*, Vol. 119. Springer Science & Business Media.

884 Doedel, E. J., 2007: Lecture notes on numerical analysis of nonlinear equations. *Numerical*
885 *Continuation Methods for Dynamical Systems: Path following and boundary value problems*,
886 1–49.

887 Fabiani, G., F. Calabò, L. Russo, and C. Siettos, 2021: Numerical solution and bifurcation analysis
888 of nonlinear partial differential equations with extreme learning machines. *Journal of Scientific*
889 *Computing*, **89**, 1–35.

890 Ferreira, D., J. Marshall, and J.-M. Campin, 2010: Localization of deep water formation: Role
891 of atmospheric moisture transport and geometrical constraints on ocean circulation. *Journal of*
892 *Climate*, **23** (6), 1456–1476.

893 Ferreira, D., and Coauthors, 2018: Atlantic-Pacific asymmetry in deep-water formation. *Annual*
894 *Review of Earth and Planetary Sciences*, **46** (1), 1–26.

895 Ford, H. L., N. J. Burls, P. Jacobs, A. Jahn, R. P. Caballero-Gill, D. A. Hodell, and A. Fedorov,
896 2022: Sustained mid-Pliocene warmth led to deep water formation in the North Pacific. *Nature*
897 *Geoscience*, 1–6.

898 Fučkar, N. S., and G. K. Vallis, 2007: Interhemispheric influence of surface buoyancy conditions
899 on a circumpolar current. *Geophysical research letters*, **34** (14).

900 Galbraith, E. D., and Coauthors, 2011: Climate variability and radiocarbon in the CM2Mc earth
901 system model. *Journal of Climate*, **24** (16), 4230–4254.

902 Gent, P. R., and J. C. Mcwilliams, 1990: Isopycnal mixing in ocean circulation models. *Journal of*
903 *Physical Oceanography*, **20** (1), 150–155.

904 Gnanadesikan, A., 1999: A simple predictive model for the structure of the oceanic pycnocline.
905 *Science*, **283** (5410), 2077–2079.

906 Gnanadesikan, A., R. Kelson, and M. Sten, 2018: Flux correction and overturning stability:
907 Insights from a dynamical box model. *Journal of Climate*, **31** (22), 9335–9350.

908 Gnanadesikan, A., M.-A. Pradal, and R. Abernathey, 2015: Exploring the isopycnal mixing and
909 helium–heat paradoxes in a suite of earth system models. *Ocean Science*, **11** (4), 591–605.

910 Hahn, L. C., K. C. Armour, M. D. Zelinka, C. M. Bitz, and A. Donohoe, 2021: Contributions to
911 polar amplification in CMIP5 and CMIP6 models. *Frontiers in Earth Science*, **9**, 710 036.

912 Hallberg, R., and A. Gnanadesikan, 2001: An exploration of the role of transient eddies in
913 determining the transport of a zonally reentrant current. *Journal of Physical Oceanography*,
914 **31** (11), 3312–3330.

915 Huang, R. X., J. R. Luyten, and H. M. Stommel, 1992: Multiple equilibrium states in combined
916 thermal and saline circulation. *Journal of physical oceanography*, **22** (3), 231–246.

917 Johnson, G. C., and H. L. Bryden, 1989: On the size of the antarctic circumpolar current. *Deep*
918 *Sea Research Part A. Oceanographic Research Papers*, **36** (1), 39–53.

919 Johnson, H. L., P. Cessi, D. P. Marshall, F. Schloesser, and M. A. Spall, 2019: Recent contributions
920 of theory to our understanding of the Atlantic meridional overturning circulation. *Journal of*
921 *Geophysical Research: Oceans*, **124** (8), 5376–5399.

922 Johnson, H. L., D. P. Marshall, and D. A. Sproson, 2007: Reconciling theories of a mechanically
923 driven meridional overturning circulation with thermohaline forcing and multiple equilibria.
924 *Climate Dynamics*, **29** (7), 821–836.

925 Jones, C. S., and P. Cessi, 2016: Interbasin transport of the meridional overturning circulation.
926 *Journal of Physical Oceanography*, **46** (4), 1157–1169.

927 Jones, C. S., and P. Cessi, 2017: Size matters: Another reason why the Atlantic is saltier than the
928 Pacific. *Journal of Physical Oceanography*, **47** (11), 2843–2859.

929 Klinger, B. A., and T. W. Haine, 2019: *Ocean circulation in three dimensions*. Cambridge Univer-
930 sity Press Cambridge.

931 Levermann, A., and J. J. Fürst, 2010: Atlantic pycnocline theory scrutinized using a coupled
932 climate model. *Geophysical Research Letters*, **37** (14), L14 602, <https://doi.org/doi:10.1029/2010GL044180>.

934 Liu, W., S.-P. Xie, Z. Liu, and J. Zhu, 2017: Overlooked possibility of a collapsed Atlantic
935 Meridional Overturning Circulation in warming climate. *Science Advances*, **3** (1), e1601 666.

936 Locarnini, R. A., and Coauthors, 2013: *Volume 1: Temperature*. World Ocean Atlas 2013, NOAA
937 Atlas NESDIS, S. Levitus, Ed., A. Mishonov Technical Ed.; NOAA Atlas NESDIS 73.

938 Lumpkin, R., and K. Speer, 2007: Global ocean meridional overturning. *Journal of Physical*
939 *Oceanography*, **37 (10)**, 2550–2562.

940 Marinov, I., A. Gnanadesikan, J. Toggweiler, and J. L. Sarmiento, 2006: The Southern Ocean
941 biogeochemical divide. *Nature*, **441 (7096)**, 964–967.

942 Nikurashin, M., and G. Vallis, 2011: A theory of deep stratification and overturning circulation in
943 the ocean. *Journal of Physical Oceanography*, **41 (3)**, 485–502.

944 Nilsson, J., P. L. Langen, D. Ferreira, and J. Marshall, 2013: Ocean basin geometry and the
945 salinification of the atlantic ocean. *Journal of Climate*, **26 (16)**, 6163–6184.

946 Park, Y.-G., and J. Whitehead, 1999: Rotating convection driven by differential bottom heating.
947 *Journal of physical oceanography*, **29 (6)**, 1208–1220.

948 Pradal, M.-A., and A. Gnanadesikan, 2014: How does the Redi parameter for mesoscale mixing
949 impact global climate in an Earth System Model? *Journal of Advances in Modeling Earth*
950 *Systems*, **6 (3)**, 586–601.

951 Rae, J. W., M. Sarnthein, G. L. Foster, A. Ridgwell, P. M. Grootes, and T. Elliott, 2014: Deep water
952 formation in the North Pacific and deglacial CO₂ rise. *Paleoceanography*, **29 (6)**, 645–667.

953 Rafter, P. A., and Coauthors, 2022: Global reorganization of deep-sea circulation and carbon
954 storage after the last ice age. *Science Advances*, **8 (46)**, eabq5434.

955 Ragen, S., K. C. Armour, L. Thompson, A. Shao, and D. Darr, 2022: The role of Atlantic basin
956 geometry in meridional overturning circulation. *Journal of Physical Oceanography*, **52 (3)**,
957 475–492.

958 Redi, M. H., 1982: Oceanic isopycnal mixing by coordinate rotation. *Journal of Physical Oceanog-*
959 *raphy*, **12 (10)**, 1154–1158.

960 Rooth, C., 1982: Hydrology and ocean circulation. *Progress in Oceanography*, **11 (2)**, 131–149.

961 Schloesser, F., 2020: The Atlantic meridional overturning circulation and the cabling effect.
962 *Journal of Physical Oceanography*, **50 (9)**, 2561–2572.

963 Sleeman, J., and Coauthors, 2023a: A generative adversarial network for climate tipping point
964 discovery (tip-gan). *arXiv preprint arXiv:2302.10274*.

965 Sleeman, J., and Coauthors, 2023b: Using artificial intelligence to aid scientific discovery of
966 climate tipping points. *arXiv preprint arXiv:2302.06852*.

967 Stommel, H., 1961: Thermohaline convection with two stable regimes of flow. *Tellus*, **13** (2),
968 224–230.

969 Talley, L. D., 1997: North Pacific Intermediate Water transports in the mixed water region. *Journal*
970 *of physical oceanography*, **27** (8), 1795–1803.

971 Toggweiler, J., and B. Samuels, 1993: Is the magnitude of the deep outflow from the Atlantic
972 Ocean actually governed by Southern Hemisphere winds? *The global carbon cycle*, Springer,
973 303–331.

974 Toggweiler, J., and B. Samuels, 1995: Effect of Drake Passage on the global thermohaline circu-
975 lation. *Deep Sea Research Part I: Oceanographic Research Papers*, **42** (4), 477–500.

976 Trenberth, K. E., Y. Zhang, J. T. Fasullo, and L. Cheng, 2019: Observation-based estimates
977 of global and basin ocean meridional heat transport time series. *Journal of Climate*, **32** (14),
978 4567–4583.

979 Tsukernik, M., and A. H. Lynch, 2013: Atmospheric meridional moisture flux over the southern
980 ocean: A story of the amundsen sea. *Journal of Climate*, **26** (20), 8055–8064.

981 Tziperman, E., J. Toggweiler, K. Bryan, and Y. Feliks, 1994: Instability of the thermohaline
982 circulation with respect to mixed boundary conditions: Is it really a problem for realistic
983 models? *Journal of Physical Oceanography*, **24** (2), 217–232.

984 Warren, B. A., 1983: Why is no deep water formed in the North Pacific? *Journal of Marine*
985 *Research*, **41** (2), 327–347.

986 Wolfe, C. L., and P. Cessi, 2011: The adiabatic pole-to-pole overturning circulation. *Journal of*
987 *Physical Oceanography*, **41** (9), 1795–1810.

988 Youngs, M. K., R. Ferrari, and G. R. Flierl, 2020: Basin-width dependence of northern deep
989 convection. *Geophysical Research Letters*, **47** (15), e2020GL089135.

990 Yu, L., X. Jin, S. A. Josey, T. Lee, A. Kumar, C. Wen, and Y. Xue, 2017: The global ocean
991 water cycle in atmospheric reanalysis, satellite, and ocean salinity. *Journal of Climate*, **30** (10),
992 3829–3852.

993 Zhang, R., and T. L. Delworth, 2005: Simulated tropical response to a substantial weakening of
994 the Atlantic thermohaline circulation. *Journal of climate*, **18** (12), 1853–1860.

995 Zweng, M., and Coauthors, 2013: *Volume 2: Salinity*. World Ocean Atlas 2013, NOAA Atlas
996 NESDIS, S. Levitus, Ed., A. Mishonov Technical Ed.; NOAA Atlas NESDIS 73.